1 *Supplement for*

2 **Enrichment of calcium in sea spray aerosol through bulk measurements and**

3 **individual particle analysis during the R/V *Xuelong* cruise over the Ross Sea,**

4 **Antarctica**

6 **By Su et al.**

8 Correspondence to: Guo-hua Zhang (zhanggh@gig.ac.cn) and Lei Li (lileishdx@163.com).

9   **Table of contents**

25   **Note:** Figures S13-S22 were used when discussing supplementary Text (S3, S5, S7, and S8) and

26   were not cited in the main-text.

27   **Introduction:** This supplement contains additional information on the comparative analysis.

Text S1. Water-soluble ion mass concentration and hygroscopicity of OC-Ca

In this study, we concluded that the OC-Ca partly accounts for the calcium enrichment over the Ross Sea, Antarctica, by combining the IGAC and SPAMS datasets.

In terms of IGAC datasets, it should be clarified that the water-soluble ion mass concentration included the pure inorganic part (e.g., pure sea salt, NaCl) and mixed organic-inorganic part (e.g., gel-like particles) (Quinn et al., 2015). Numerous studies have reported that primary sea spray aerosols (SSAs) exhibit moderate hygroscopicity and water solubility due to a certain water-soluble organic fraction (~ 25%, by mass), such as carboxylates, lipopolysaccharides (LPSs), humic substances, and galactose (Oppo et al., 1999; Quinn et al., 2015; Schill et al., 2015; Cochran et al., 2017). In particular, LPSs, which are preferentially transferred to submicron SSAs during bubble bursting, exhibit a certain solubility of 5 g L^{-1} in pure water. (Facchini et al., 2008; Schill et al., 2015). Oppo et al. (1999) indicated that humic substances are also an important pool of water-soluble natural surfactants (40-60%) in marine surfactant organic matter. Therefore, both organic and inorganic parts with a water-soluble nature could be retained, contributing to the water-soluble ion mass concentration (e.g., Ca^{2+}).

In terms of SPAMS datasets, we inferred that the OC-Ca is of biogenic origin and may be associated with marine microgels (i.e., gel-like particles). If so, these gel-like particles are most likely water-insoluble and/or slightly water-soluble (Leck and Bigg, 2010; Orellana et al., 2011). Under the stimulation of environment factors (pH, temperature, chemical compounds, pollutants, and UV radiation), their physicochemical properties would be changed (e.g., the cleavage of polymers results in enhanced water-solubility) (Orellana and Verdugo, 2003; Orellana et al., 2011). Although we did not measure the hygroscopicity of the OC-Ca particle type in this study, we

50   considered the OC-Ca to be hygroscopic to some extent, based on the results of Cochran et al. (2017).

51   Those authors concluded that the mixture of sea salt with organic matter (i.e., the single-particle

52   types of SS-OC and OC) can also exhibit a certain hygroscopicity (hygroscopicity parameter, 0.50-

53   1.27).

54   **Text S2. A brief description of the in-situ Gas and Aerosol Compositions monitoring system**

55   **and the single-particle aerosol mass spectrometer**

56   The aerosol water-soluble ion mass concentrations with an aerodynamic diameter of 10 μm

57   were provided by an in-situ Gas and Aerosol Compositions monitoring system. The detailed

58   analytical discipline and methodology were described in previous studies (Yan et al., 2019; Yan et

59   al., 2020b). Briefly, the IGAC system consisted of three main units, including a Wet Annular

60   Denuder (WAD), a Scrub and Impact Aerosol Collector (SIAC), and an ion chromatograph (IC,

61   (Dionex ICS-3000)). Gases and aerosols were passed through WAD with a sampling flow of 16.7 L

62   min^{-1}. Two concentric Pyrex glass cylinders with a length of 50 cm and inner and outer diameters

63   of 1.8 and 2.44 cm were assembled to WAD, in which the inner walls of the annulus were wetted

64   with ultrapure water (18.2 MΩ cm^{-1}). This part was responsible for the collection of acidic and basic

65   gases by diffusion and absorption of downward flowing aqueous solution. The SIAC had a length

66   of 23 cm and diameter of 4.75 cm, which was positioned at an angle to facilitate the collection of

67   enlarged particles. The collected particles were separated firstly, continually enlarged by vapor

68   steam, and then accelerated through a conical-shaped impaction nozzle and collected on an

69   impaction plate. Each aerosol sample was collected for 55 minutes and injected for 5 minutes. The

70   particles were subsequently analyzed for cations and anions by using an ion chromatography (IC)

71   system (Dionex ICS-3000). The injection loop size was 500 μL for both anions and cations. The

72   target ion concentrations were calibrated with a coefficient of determination (r^2) above 0.99 by using

73   standard solutions (0.1-2000 μg L^{-1}). The detection limits for Na, Cl, Ca, K, and Mg were 0.03, 0.03,

74   0.019, 0.011, and 0.042 μg L^{-1} (aqueous solution), respectively. The systematic error of the IC

75   systems was generally less than 5%.

76   Single-particle mass spectral fingerprints and vacuum aerodynamic diameter (D_{va}) lengths

77   ranging from 0.2 to 2 μm were provided by SPAMS (Li et al., 2011). Briefly, the aerosols were

78   drawn into an aerodynamic lens, forming a collimated particle beam and were then accelerated in

79   an accelerating electric field and passed through two continuous laser beams (Nd: YAG laser, 532

80   nm). The obtained time of flight (TOF) and velocity of individual particles were used to calculate

81   the D_{va} based on a calibration curve. Subsequently, particles with a specific velocity were desorbed

82   and ionized by triggering a pulse laser (an Nd: YAG laser, 266 nm, 0.6 ± 0.06 mJ was used in this

83   study). The ion fragments were recorded using a TOF mass spectrometer. Prior to the use of SPAMS,

84   standard polystyrene latex spheres (Duke Scientific Corp., Palo Alto, CA) and $PbCl_2$ and $NaNO_3$

85   (Sigma-Aldrich) were used for the size and mass spectral calibration, respectively.

Text S3. Uncertainty analysis and quality assurance of datasets

87   **IGAC:** The water-soluble ion mass concentrations were analyzed by using an ion

88   chromatography (IC) system (Dionex ICS-3000) within an in-situ Gas and Aerosol Compositions

89   monitoring system (IGAC, Model S-611). Before the sampling, a known concentration of LiBr was

90   used as an internal standard by adding to the aerosol liquid samples to determine the stability of the

91   IGAC system. The changes in the internal standard were within 5%. Subsequently, the IC was

92   calibrated by using six to eight concentrations of stand solutions (0.1-2000 μg L^{-1}), depending on

93   the target species and concentrations, in which the R^2 was above 0.99. The calibration curves for

94   each ion could be found in our previous studies (Yan et al., 2019; Yan et al., 2020a; Yan et al., 2020b).

95   The uncertainty of the IC systems was generally less than 5% for all analyzed ionic species. The

96   detection limits for Na^+, Cl^-, Ca^{2+}, K^+, and Mg^{2+} were 0.03, 0.03, 0.019, 0.011, and 0.042 μg L^{-1}

97   (aqueous solution), respectively. During the whole sampling period (hourly temporal resolution),

98   the detection rate for Na^+, Cl^-, Ca^{2+}, K^+, and Mg^{2+} were 98.5% (1178 of 1196), 92.6% (1108 of

99   1196), 88.2% (1055 of 1196), 98.9% (1183 of 1196), and 98.5% (1178 of 1196), respectively. All

100   values below the detection limit were omitted before analysis. The undetected rate for both Ca^{2+} and

101   Na^+ was approximately 12%. Figure S13 shows the time series of observed ion mass concentrations

102   and EF_{Ca}. The ion mass concentrations were above the detection limit. Particularly, the mean Na^+

103   and Ca^{2+} mass concentrations were 364.64 ng m^{-3} (ranging from 6.66 to 4580.10 ng m^{-3}) and 21.20

104   ng m^{-3} (ranging from 0.27 to 334.40 ng m^{-3}), respectively, which were far above (> 10 times) the

105   detection limit. Such data indicate that the variations of EF_{Ca} would not suffer the increasing

106   uncertainties when the ion mass concentrations near the detection limit. Thus, we suggest that the

107   data on ion mass concentration is reliable and representative.

108   Given that the measured mass concentrations of Ca^{2+} and Na^+ were far above the detection

109   limit, we only considered the systematic errors (< 5%) of the mass concentrations of Ca^{2+} and Na^+.

110   Based on the variations of extreme value, the uncertainty of each EF_{Ca} is calculated as below:

111   $$abs(1 - \frac{\frac{0.95 * Ca^{2+}_{conc.}}{1.05 * Na^+_{conc.}}/0.038}{\frac{Ca^{2+}_{conc.}}{Na^+_{conc.}}/0.038}) \approx 9.5\% < Unc_{(EFCa)} < abs(1 - \frac{\frac{1.05 * Ca^{2+}_{conc.}}{0.95 * Na^+_{conc.}}/0.038}{\frac{Ca^{2+}_{conc.}}{Na^+_{conc.}}/0.038}) \approx 10.5\%$$

112   Where $Ca^{2+}_{conc.}$ and $Na^+_{conc.}$ represent the observed ion mass concentration of Ca^{2+} and Na^+,

113   respectively. 0.038 is the ratio of Ca^{2+} to Na^+ in seawater. 0.95 and 1.05 represent the variations of

114   extreme value. The largest uncertainty of EF_{Ca} ($Unc_{(EFCa)}$) would be estimated lower than 11%.

115   **SPAMS:** Even though SPAMS has advantages for investigating the chemical characteristics

116   and evolutionary mechanisms of individual particles, it is still quite challenging for it to provide

117   quantitative evidence, as it is limited by the potential matrix effects, laser inhomogeneities, and

118   transmission efficiencies of the aerodynamic lenses (Qin et al., 2006; Pratt and Prather, 2012).

119   Nevertheless, the results via SPAMS are also reliable because of its broad datasets with high

120   temporal resolution. Therefore, the analyses of particle count, size, and chemical composition (by

121   peak area) can be considered semi-quantitative from a statistical perspective (Healy et al., 2012; Su

122   et al., 2021a; Zhang et al., 2021).

123   **Results:** The results of the Ca^{2+}, K^+, and Mg^{2+} enrichment in SSAs calculated by ion mass

124   concentration (via IGAC) are not fully supported by SPAMS datasets, which is not surprising. We

125   propose three possible explanations for these results: (i) There is a difference in the size of collected

126   particles between SPAMS (0.2–2 μm) and IGAC (~ 10 μm). In addition, SPAMS cannot measure

127   the Aitken-mode particles and measures only the tail of accumulation-mode particles (Sierau et al.,

128   2014). The hit rate of the SPAMS when measuring particles was relatively low (~ 11%). (ii) The

129   obtained type via IGAC (ion mass concentration) and SPAMS (mass spectral characteristics)

130   datasets are different. In particular, the datasets via SPAMS are semiquantitative due to the potential

131   matrix effects, laser inhomogeneities, and transmission efficiencies of the aerodynamic lens. (iii)

132   IGAC can only measure the water-soluble Ca^{2+}, however, the water solubility of OC-Ca may be low.

133   Although there is a discrepancy between the two instruments, we consider our results to be

134   reliable and representative. The quantitative results concluded by IGAC verify the enrichment of

135   Ca^{2+}, K^+, and Mg^{2+} in the SSAs and subsequently reveal their dependence on and relevance to the

136   environmental factors. Previous studies have shown increasing Ca^{2+} enrichment in SSAs below 1

137   μm (Oppo et al., 1999; Hara et al., 2012; Cochran et al., 2016; Salter et al., 2016; Mukherjee et al.,

138   2020). Thus, the individual particle analysis of particle types ranging in size from 0.2 to 2 μm is

139   very appropriate for revealing the calcium distribution in SSAs. Our results successfully identify a

140   unique calcareous particle type (i.e., OC-Ca) and its specific mixing state, which provides some

141   qualitative and semi-quantitative insights into the mechanisms behind calcium enrichment.

142   **Text S4. Single-particle characteristics of other observed particles**

143   In this study, a total of ~ 930, 000 particles with mass spectral information and D_{va} were

144   measured using SPAMS and manually clustered into the seven single-particle groups of SS (sea salt

145   aerosol), SS-aged (aged sea salt aerosol), SS-Bio (sea salt with biogenic organic matter), OC-Ca

146   (internally mixed organics with calcium), OC-K (internally mixed organics with potassium), OC

147   (organic-carbon-dominated), and EC (element carbon) (Table S2). Based on their different mass

148   spectral characteristics (Prather et al., 2013; Collins et al., 2014; Guasco et al., 2014; Su et al.,

149   2021b), we briefly describe all of them (except for OC-Ca) as follows (Figure S5):

150   SS is identified by prominent ion markers that are associated with Na and Cl (e.g., m/z 23 $[Na]^+$,

151   46 $[Na_2]^+$, 81 $[Na_2{}^{35}Cl]^+$, 83 $[Na_2{}^{37}Cl]^+$, -35 $[{}^{35}Cl]^-$, and -37 $[{}^{37}Cl]^-$), and smaller contributions of

152   other inorganic matter that are known to exist in sea water (i.e., Mg, K, Ca). SS accounted for 16.5%

153   of the particles obtained during the observation cruise, with a peak of ~ 1.25 μm in D_{va}.

154   SS-aged can be regarded as SS with atmospheric aging, with additional characteristic peaks of

155   nitrate (m/z -46 $[NO_2]^-$ and -62 $[NO_3]^-$). SS-aged presented a similar size distribution as SS, with a

156   proportion of 8.1%.

SS-Bio is characterized by a large ratio of organic ion signatures of organic nitrogen (m/z -26 [CN]$^-$ and -42 [CNO]$^-$), phosphate (m/z -63 [PO$_2$]$^-$ and -79 [PO$_3$]$^-$), carbohydrate (m/z -45 [CHO$_2$]$^-$, -59 [C$_2$H$_3$O$_2$]$^-$, and -73 [C$_3$H$_5$O$_2$]$^-$), siliceous materials (m/z -60 [SiO$_2$]$^-$), and organic carbon (m/z 27 [C$_2$H$_3$]$^+$ and 43 [C$_2$H$_3$O$_3$]$^+$), in addition to the aforementioned inorganic salt-related ion signature (e.g., 23 [Na]$^+$). SS-Bio accounted for only 3.1% of the particles obtained during the observation cruise, with a peak of ~ 0.9 μm in D_{va}.

OC-K is identified by the dominant presence of K (m/z 39) and the aforementioned organic species and exhibited the third largest proportion (13.7%). OC-K was scattered in the D_{va} range of 0.2 to1.0 μm, peaking at 0.6 μm. Similar to OC-Ca, this chemical class may also be associated with biogenic origin, which may originate from intact heterotrophic bacterial cells, fragments of cells, and bacterial exudates (Gaston et al., 2011; Guasco et al., 2014; Sierau et al., 2014).

OC exhibits a significant proportion of organic signals of organic carbon and organic nitrogen. This single-particle type may originate from not only heterogeneous nucleation with the oxidation of monoterpene and isoprene but also anthropogenic emissions (e.g., ship emissions). However, we suggest that it is more likely to be related to the biogenic origin of the bacteria and phytoplankton.

Text S5. Potassium (K$^+$) and magnesium (Mg^{2+}) enrichment in SSAs induced by temperature, wind speed, and sea ice

The enrichment factors of K$^+$ (EF$_K$) and Mg^{2+} (EF$_{Mg}$) were calculated by using the same equation described in the main text. Generally, the ratios of K$^+$ and Mg^{2+} to Na$^+$ in seawater are 0.0218 and 0.1112, respectively (Hara et al., 2012; Boreddy and Kawamura, 2015; Su et al., 2022). During the observation cruise, EF$_K$ (ranging from 0.20 to 75, with a median and mean of 1.19

178   and 3.61, respectively, n > 1000) and EF_{Mg} (ranging from 0.12 to 26.94, with a median and mean of

179   1.48 and 2.46, respectively, n > 1000) were also observed.

180   Figure S14 shows the enrichment factors of K^+ and Mg^{2+} with respect to sodium in bulk

181   aerosols at different ambient temperatures (≥ -3.5°C and < -3.5°C), wind speeds (≥ 7 m s^{-1} and < 7

182   m s^{-1}), and sea ice fraction (with and without sea ice) during the whole sampling period. The results

183   were very similar to that of calcium (Ca^{2+}) enrichment in SSAs, which may present an analogous

184   enrichment mechanism by environmental factors (e.g., ambient temperature and wind speed with

185   sea ice) (Fig. S15).

186   We also inferred that the K^+ and Mg^{2+} enrichments in SSAs were also attributed to organically

187   internally mixed aerosols (e.g., OC-K and SS-Bio). We propose three possible explanations for this:

188   (i) If the released K^+ and Mg^{2+} are in the form of inorganic salts (e.g., KCl and $MgCl_2$) within SSAs,

189   they are likely to be associated with sea salt fractionation by precipitations of sylvite ca. -33°C and

190   10 $H_2O·MgCl_2$ ca. -36°C on the sea ice (Hara et al., 2012). However, the average and minimum

191   ambient temperatures during leg I were only -4.1 °C and ~ -8 °C, respectively. Thus, sea salt

192   fractionation on sea ice is less likely. (ii) We observed a single-particle type of OC-K with abundant

193   K^+ (*m/z* 39) and organic ion signatures by using SPAMS during the cruise observations. Other

194   single-particle types involving K^+ (*m/z* 39) and Mg^{2+} (*m/z* 24) also exhibited some characteristic

195   organic peaks (e.g., in SS-Bio). (iii) K^+ and Mg^{2+} are also greatly capable of stabilizing organic

196   supramolecular structures in the form of organic ligands (i.e., marine microgels) (Gaston et al., 2011;

197   Cochran et al., 2016; Mukherjee et al., 2020). Based on the above discussion, we therefore suggest

198   that internally mixed potassium and magnesium organics contribute to corresponding enrichment in

199   SSAs. Analogous to OC-Ca, we also suggest that the marine microgels assembled by K^+ and Mg^{2+}

200   to exopolymer substances (EPSs) may be emitted to the atmosphere by low wind-blown sea ice.

201   **Text S6. Further correlation analysis between mass concentration of Ca^{2+}, single-particle type**

202   **of OC-Ca, and single-particle type of SS**

203   We noted there was a relatively poor correlation (r = 0.51, $p < 0.05$) between sodium and

204   calcium mass concentrations, probably indicating some differences in their origin, chemical form,

205   and water solubility (Fig. S9). As discussed in the main text, we concluded that there were four

206   possible origins for water-soluble Ca^{2+} collected by IGAC, including (1) sea salt fractionation (i.e.,

207   ikaite, $CaCO_3 \cdot 6H_2O$), (2) long-range transport of dust or anthropogenic emissions, (3) coexistence

208   with sea salt aerosol (i.e., the single-particle type of SS-Ca) and (4) calcium internally mixed

209   organics (OC-Ca). The first two origins were excluded based on the discussion in the main text and

210   Text S4.

211   In terms of the third possible origin (i.e., coexistence with sea salt aerosols), we noted that there

212   were relatively poor correlations between the SS-Ca (r = 0.21, $p < 0.05$, by count and r = 0.03, $p <$

213   0.05, by peak area of m/z 40 $[Ca]^+$) and mass concentration of Ca^{2+} (Table S5). This indicated that

214   the single-particle type of SS-Ca had a certain contribution to the water-soluble mass concentration

215   of Ca^{2+}. We suggest that this part of calcium is inorganic and water-soluble because we did not

216   observe organic signals (e.g., organic nitrogen, phosphate, and carbohydrate). This may not be the

217   major reason for the Ca^{2+} enrichment in SSA.

218   We suggest that OC-Ca may be important for the higher EF_{Ca} observed, which is supported by

219   the increased correlations between the OC-Ca (by count and by peak area of m/z 40 $[Ca]^+$) and mass

220   concentration of Ca^{2+} that varied with increasing EF_{Ca} (Table S5). Considering the possible influence

221   of water-soluble components (e.g., $CaCl_2$, $Ca(NO_3)_2$, and $CaSO_4$), we classified OC-Ca into two

222   parts: OC-Ca-Organic (~ 147, 000, by count) and OC-Ca-Inorganic (~ 283, 000, by count) (Fig.

223   S12). Compared to the former, the latter presented typical inorganic ion characteristic peaks of

224   chloride (m/z -35 and -37), nitrate (m/z -62), and sulfate (m/z -97) and was probably more water-

225   soluble. We noted that both presented similar variations in which the correlations between the OC-

226   Ca (by count and by peak area of m/z 40 $[Ca]^+$) and mass concentration of Ca^{2+} varied with

227   increasing EF_{Ca} (Table S5). However, OC-Ca-Organic exhibited stronger correlations than did OC-

228   Ca-Inorganic (r = 0.51 vs. r = 0.28, $p < 0.05$, by count and r = 0.51 vs. 0.31, $p < 0.05$, by peak area

229   of m/z 40 $[Ca]^+$, respectively), which may emphasize the importance of OC-Ca-Organic to the

230   enrichment of Ca^{2+}. That is, the potential contribution of organically complexed calcium may be

231   ignored, when considering the calcium enrichment in SSAs based on water-soluble Ca^{2+}.

232   Direct measuring the hygroscopicity of the OC-Ca remained a technical challenge in this study.

233   Nevertheless, we could infer that OC-Ca was hygroscopic to some extent, based on the results from

234   Cochran et al. (2017), because they concluded that the mixture of sea salt with organic matter (i.e.,

235   the single-particle type of SS-OC and OC) can also exhibit a certain hygroscopicity (hygroscopicity

236   parameter, 0.50-1.27).

237   **Text S7. Multiple linear and random forest regression**

238   Multiple linear and random forest analyses were applied to describe the relative contribution

239   of possible factors to the variations in EF_{Ca}. In multiple linear models, two of the most common

240   measures of model fit are the residual standard error and proportion of variance explained (R^2), by

241   using least squares fit. In contrast, random forest with nonlinear multiple regression has been widely

242 applied to predict and reproduce the importance of factors, by building multiple decision trees

243 (Lundberg et al., 2020; Zhang et al., 2021; Song et al., 2022).

244   We attempted to estimate the relative importance of the impact factors on EF_{Ca}, including the

245 environmental factors (ambient temperature, wind speed, and chlorophyll-a concentration), particle

246 types (SS-Ca and OC-Ca, by count), and relative fraction of organics in the OC-Ca particles. The

247 multiple linear regression and random forest analysis were applied. As shown in Fig. S16, EF_{Ca}

248 could not be well predicted by those possible factors for the sea ice period ($r^2 = 0.19$, $p < 0.01$) and

249 whole sampling period ($r^2 = 0.15$, $p < 0.01$), which may be ascribed to other unknown mechanisms

250 and/or OC-Ca with low water solubility. Future studies are needed to explore the mechanisms of

251 calcium enrichment in SSAs.

252 **Text S8. A comparative analysis of chemical composition, particle size and counts, and mixing**

253 **state via SPAMS between leg I and leg II**

254   Based on the SPAMS datasets, we found that there was a minimal change in chemical

255 composition (Figs. S17 and S18), particle size (Fig. S19) and counts (Fig. S20), and mixing state

256 (Figs. S21 and S22) of the obtained particles (especially SS-Bio, OC-Ca, and OC-K) during leg I

257 (sea ice period) and leg II (period without Sea ice). This suggests that the existence of sea ice may

258 play an insignificant role in the intrinsic physicochemical properties of the obtained particles

259 ranging from 0.2 to 2 μm.

260

261 **2. Supplementary Figures**
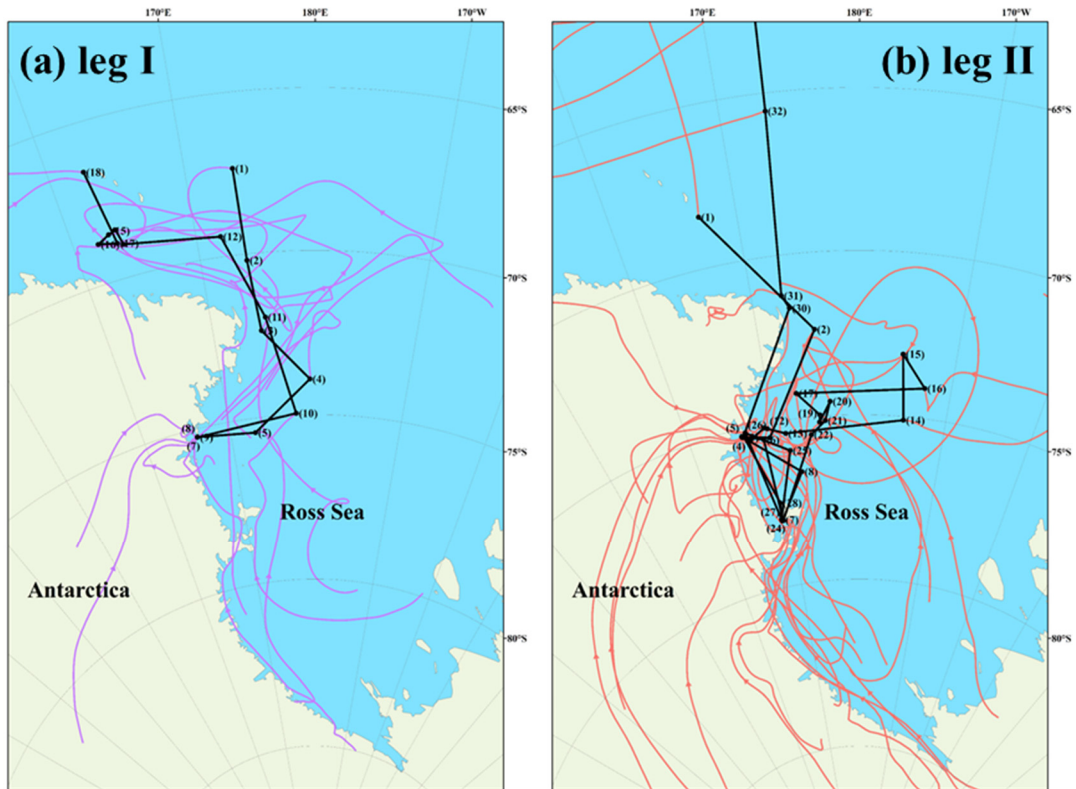
262

263 Figure S1

264 HYSPLIT back trajectories (72) arriving at the ship location (50 m above sea level) every day (0:00

265 local time) during leg I (purple solid line) and leg II (red solid-line). The black solid-lines indicate

266 the cruise track of the R/V *Xuelong*. The marked numbers indicate the ship location at the local time

267 0:00 during the whole observation. For example, "(1)" in leg I refers to the ship location at 0:00, on

268 2 December 2017, and so on.
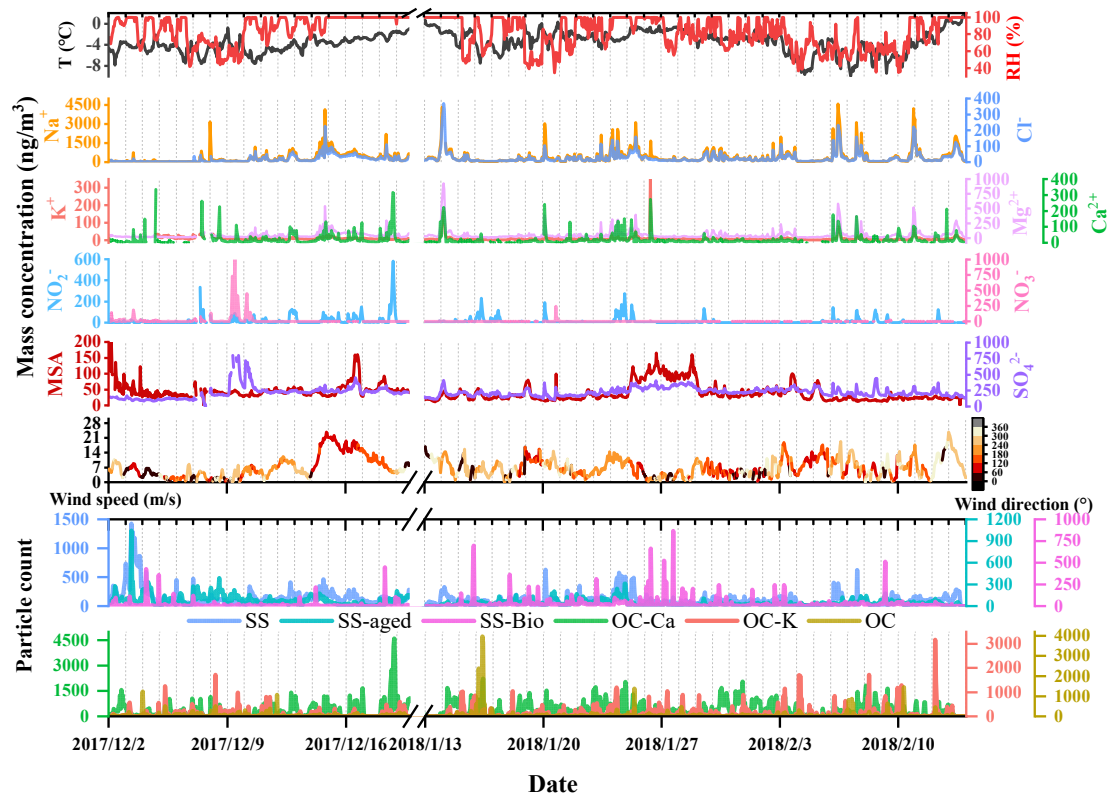
269

270 Figure S2

271 Time series (hourly temporal resolution) of meteorological parameters, typical water-soluble ion

272 mass concentrations, and single-particle counts of individual particle types.
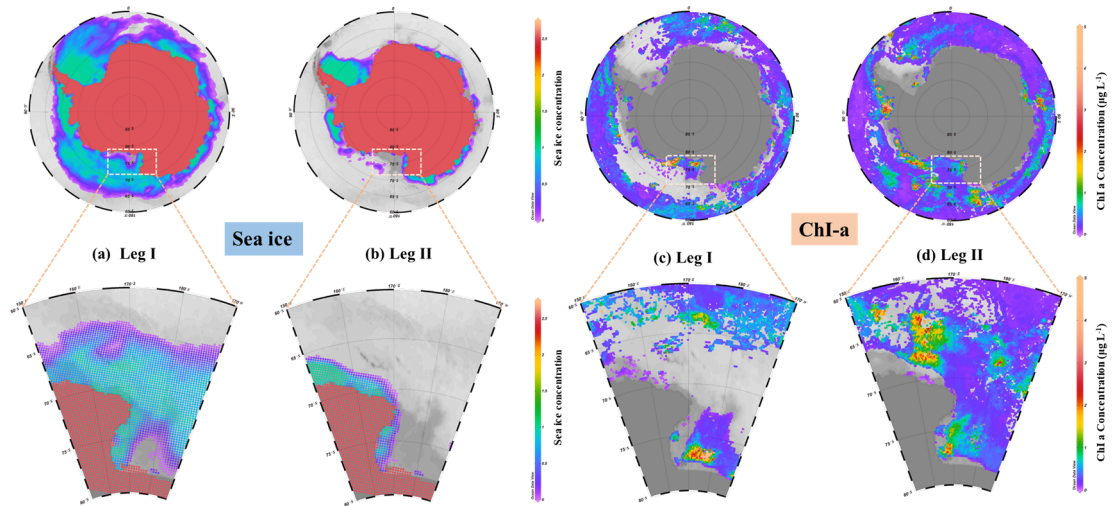
273

274   Figure S3

275   Average sea ice fraction and chlorophyll-a concentration during leg I (a and c) and leg II (b and d)

276   from a satellite. This figure was created by using Ocean Data View (Schlitzer, 2002).

277

278 Figure S4

279 An in situ Gas and Aerosol Composition monitoring system (IGAC) was used to determine the

280 gaseous and aerosol water-soluble ion mass concentrations (red frame, left). A Single Particle

281 Aerosol Mass Spectrometer (SPAMS) was used to measure the chemical compositions, mixing

282 states and particle size of individual particles (green frame, right).
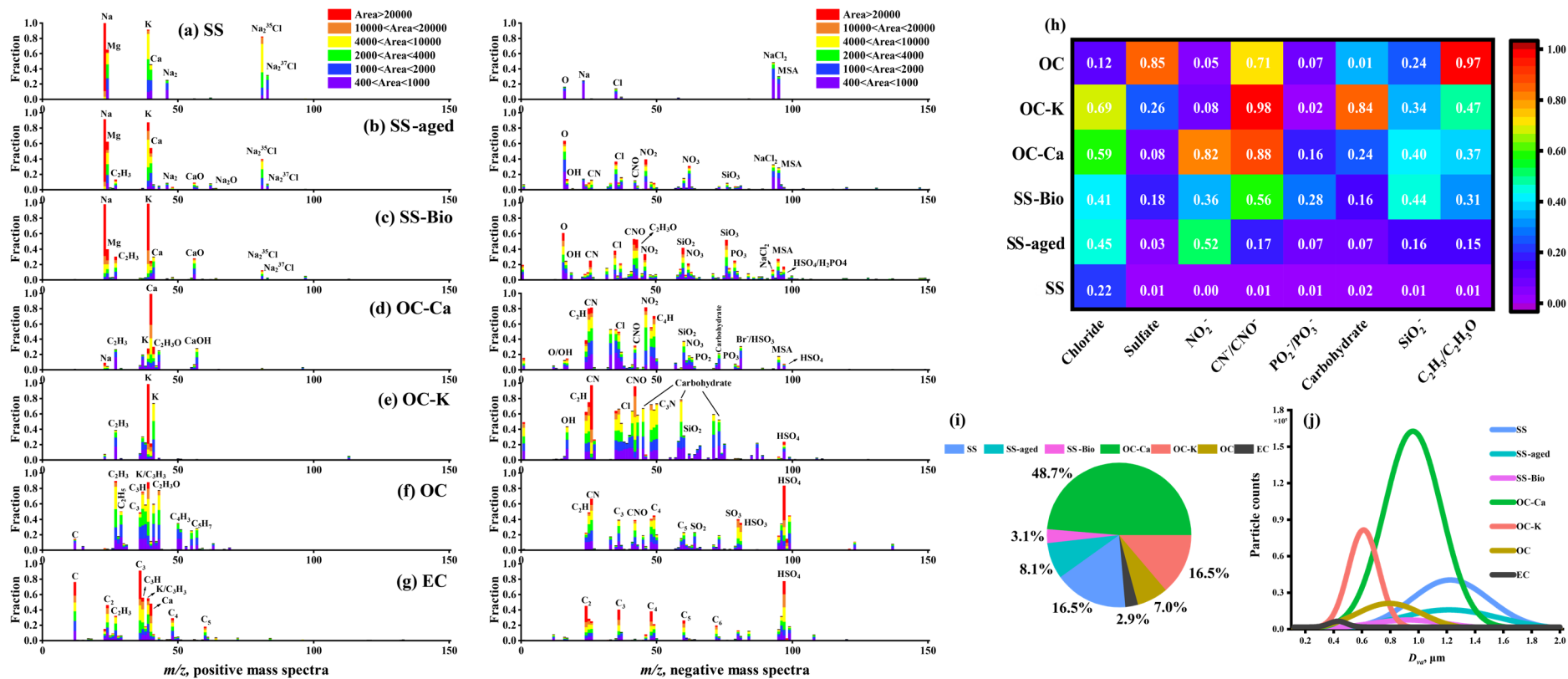
283

284 Figure S5

285 (a) – (g) Average digitalized single-particle mass spectra for seven classes of collected particles. (h) Hot plot of number fractions for major species of obtained single-

286   particle types, including chloride (m/z -35 and -37), sulfate (m/z -97) , nitro-containing organic species (m/z -46), organic nitrogen (m/z -26 or -42), phosphate (m/z -63

287   or -79), carbohydrate (m/z -45, -59, or -73), siliceous materials (m/z -60), and organic carbon (m/z -27 or 43). (i) Relative proportion of different single-particle types

288   during the cruise observations. (j) Unscaled size-resolved number distributions of all individual particles.

289   A total of ~ 580, 000 calcium-containing particles (m/z 40 [Ca]$^{+}$) were observed during cruise observations, accounting for ~ 62% of the total obtained particles.

290   These calcium-containing particles were scattered among all the obtained particle types, with proportion of ~48%, ~56%, ~25%, ~22%, ~100%, ~12%, and ~49% for

291   SS, SS-aged, SS-Bio, OC-K, OC-Ca, OC, and EC, respectively. In particular, the SS-Ca and OC-Ca particle types accounted for ~ 12% and ~ 72% of the total of

292   calcium-containing particles and ~ 7% and ~ 50% of the total obtained particles, respectively.
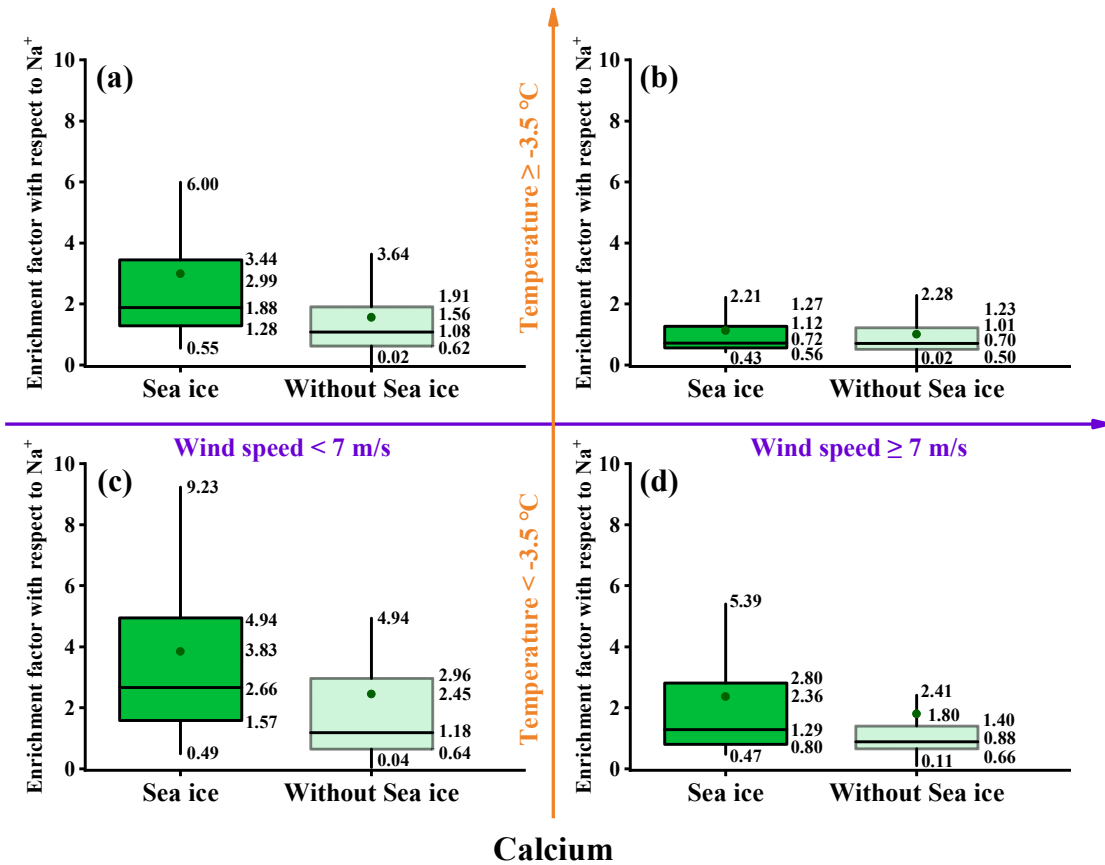
293

294 Figure S6

295 A box and whisker plot of hourly Ca^{2+} enrichment factors (EF_{Ca}) with respect to Na^+ at different

296 ambient temperatures, wind speeds, and sea ice fraction. In the box and whisker plots, the marked

297 values from top to bottom are the 90th and 75th percentiles, mean, median, and 25th and 10th

298 percentiles, respectively.

299 In comparison with the bubble charts (Fig. 1 in main text), the box and whisker plot present similar

300 intensions in different forms.
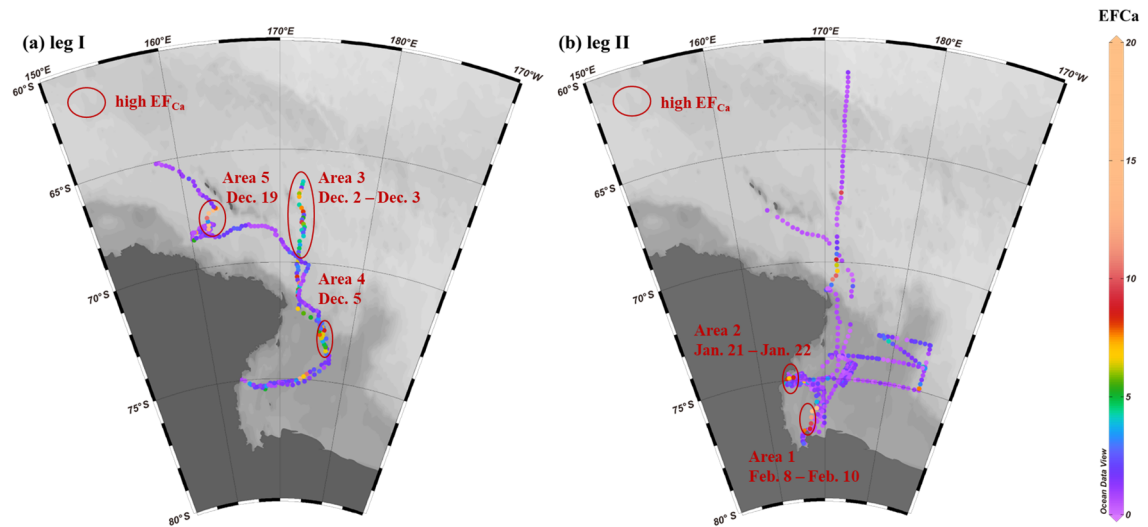
301

302   Figure S7

303   A comparative analysis of the EF_{Ca} values between leg I and leg II of the R/V *Xuelong* cruise over

304   the Ross Sea, Antarctica. We manually classified the five high EF_{Ca} areas (marked in red), which

305   could be seen in detail in Table S4.
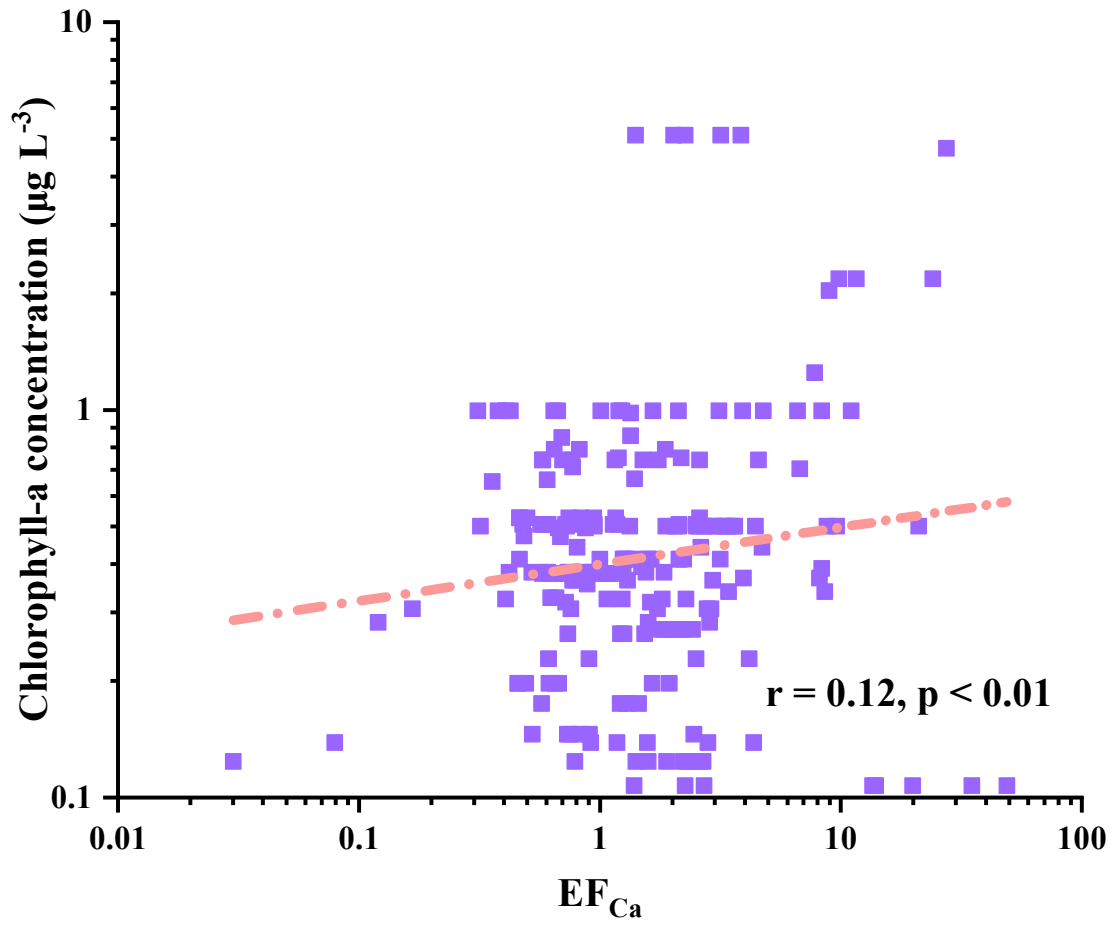
306

307   Figure S8

308   Correlation analysis between EF_{Ca} and chlorophyll-a concentration during leg II.
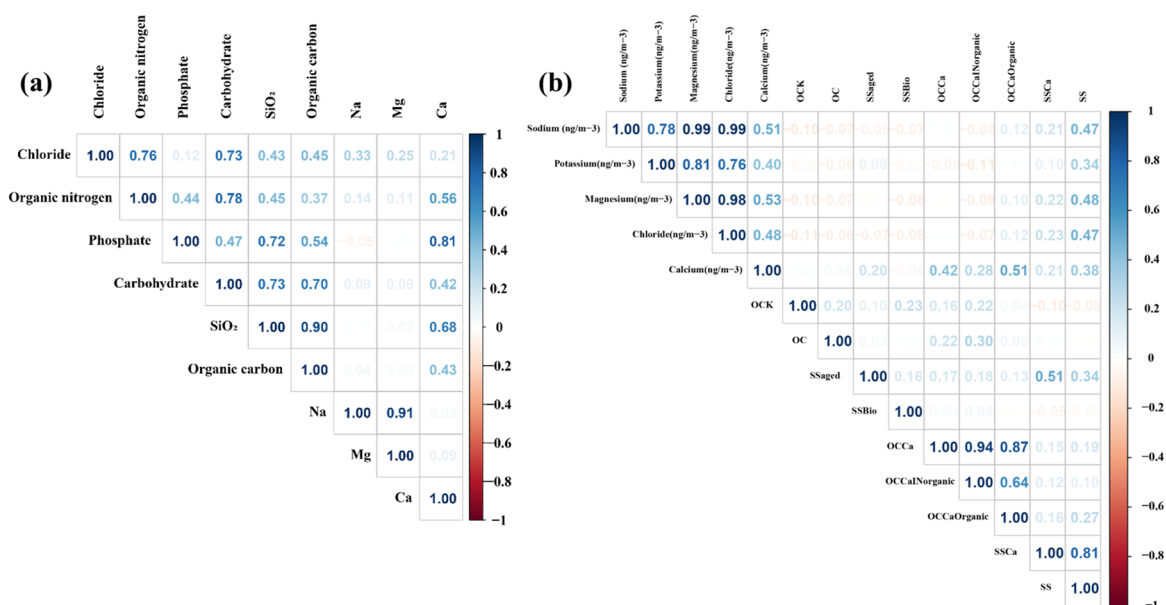
309

310 Figure S9

311 (a) Correlation analysis between the single-particle peak area for species in OC-Ca. There are

312 relatively high correlation coefficients (r = 0.42–0.81) between the peak area of Ca and organic

313 species (organic nitrogen, phosphate, carbohydrate, siliceous materials, and organic carbon). (b)

314 Correlation analysis between the OC-Ca (by count) and mass concentration of Ca^{2+}. The first

315 (sodium) to fifth (chloride) refer to mass concentration. The sixth (OCK) to fourteenth (SS) refer to

316 single-particle types.

317
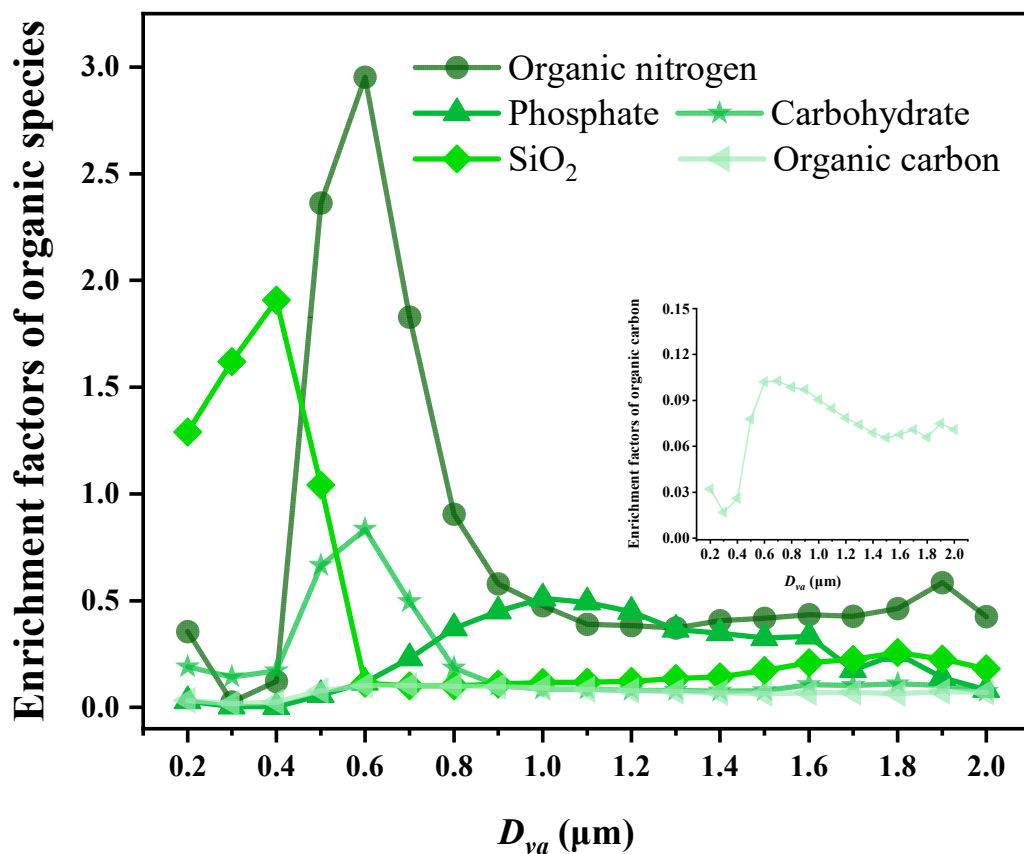
318

319   Figure S10

320   Size-dependent single-particle peak area ratio of organic matter to calcium. Based on SPAMS, we

321   define the organic matter enrichment factors as the single-particle peak area ratio of organic species

322   to Ca (*m/z* 40) in OC-Ca. The single-particle counts of OC-Ca are 420, 000. The organic species

323   include organic nitrogen (*m/z* -26 and -42), phosphate (*m/z* -63 and -79), carbohydrate (*m/z* -45, -59,

324   and -73), siliceous materials (SiO_2, *m/z* -60), and organic carbon (*m/z* 27 and 43).

325
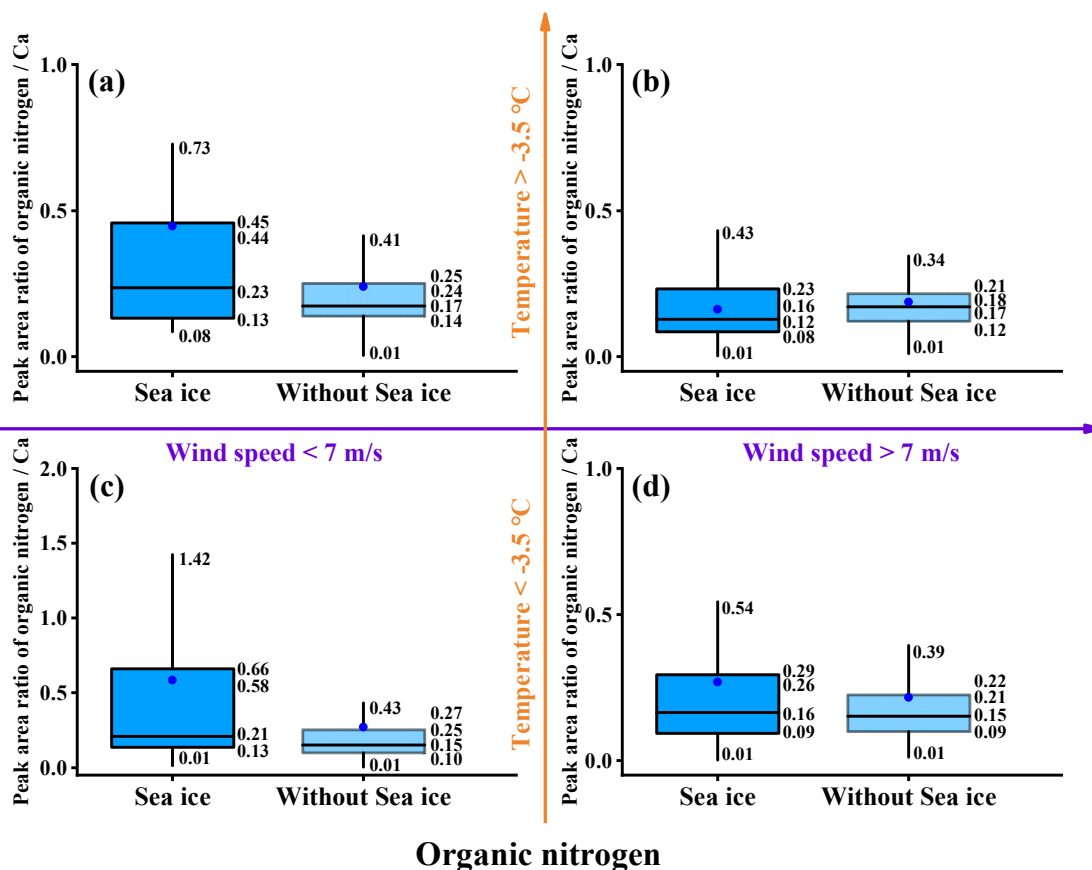
Organic nitrogen

Figure S11

A box and whisker plot of the peak area ratio of organic nitrogen (*m/z* -26 and -42) to Ca (*m/z* 40) in OC-Ca at different ambient temperatures, wind speeds, and sea ice fraction. As described above, the organic nitrogen enrichment factor in OC-Ca (EF$_{ON}$) is defined as the single-particle peak area ratio of organic nitrogen to calcium. We chose the organic nitrogen within OC-Ca for comparative analysis because of its large number fraction (0.88). In the box and whisker plot, the marked values from top to bottom are 90th and 75th percentiles, mean, median, and 25th and 10th percentiles, respectively.

335
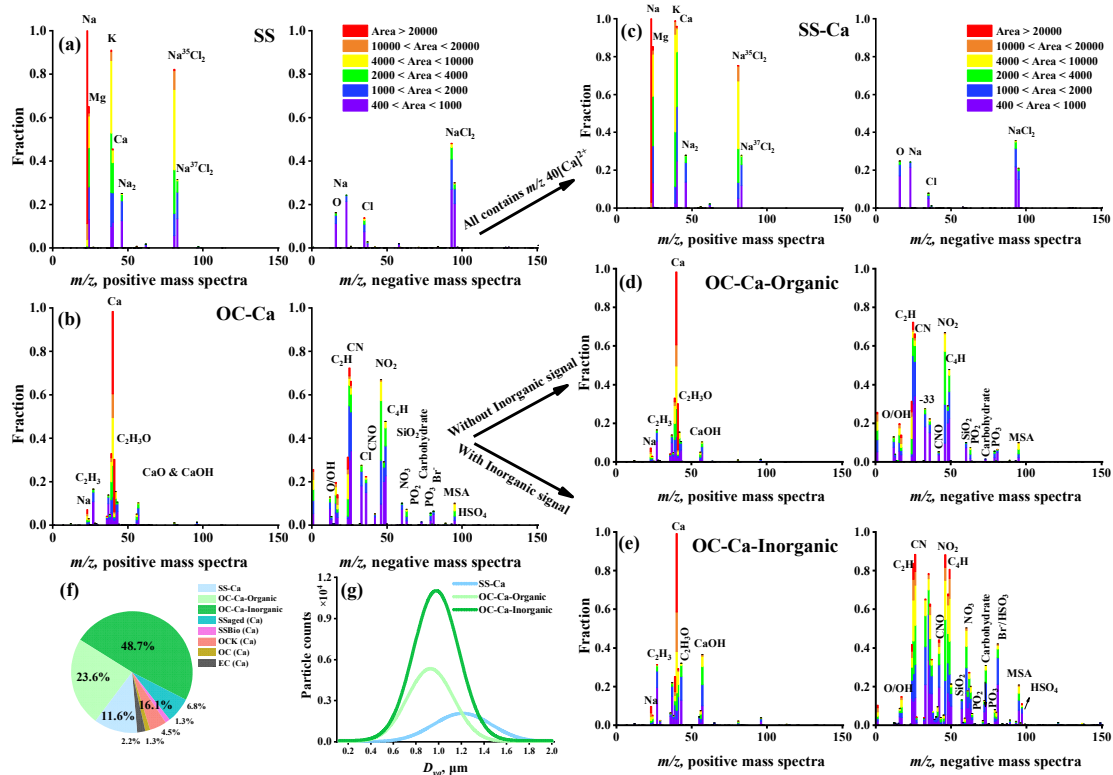
Figure S12

(a) and (b) Average digitalized single-particle mass spectra of chemical classes of SS and OC-Ca.

(c) Average digitalized single-particle mass spectra of SS-Ca that are refined by using m/z 40 $[Ca]^{2+}$

upon SS. (d) and (e) Average digitalized single-particle mass spectra of OC-Ca-Organic and OC-

Ca-Inorganic, which are classified by whether inorganic compounds (chloride (m/z -35 and -37),

nitrate (m/z -62), and sulfate (m/z -97) ion signals are present. (f) Relative proportion and (g)

unscaled size-resolved number distributions of single-particle types.

343 **Note:** Figures S13-S22 were used when discussing supplementary Text (S3, S5, S7, and S8) and

344 were not cited in the main-text.
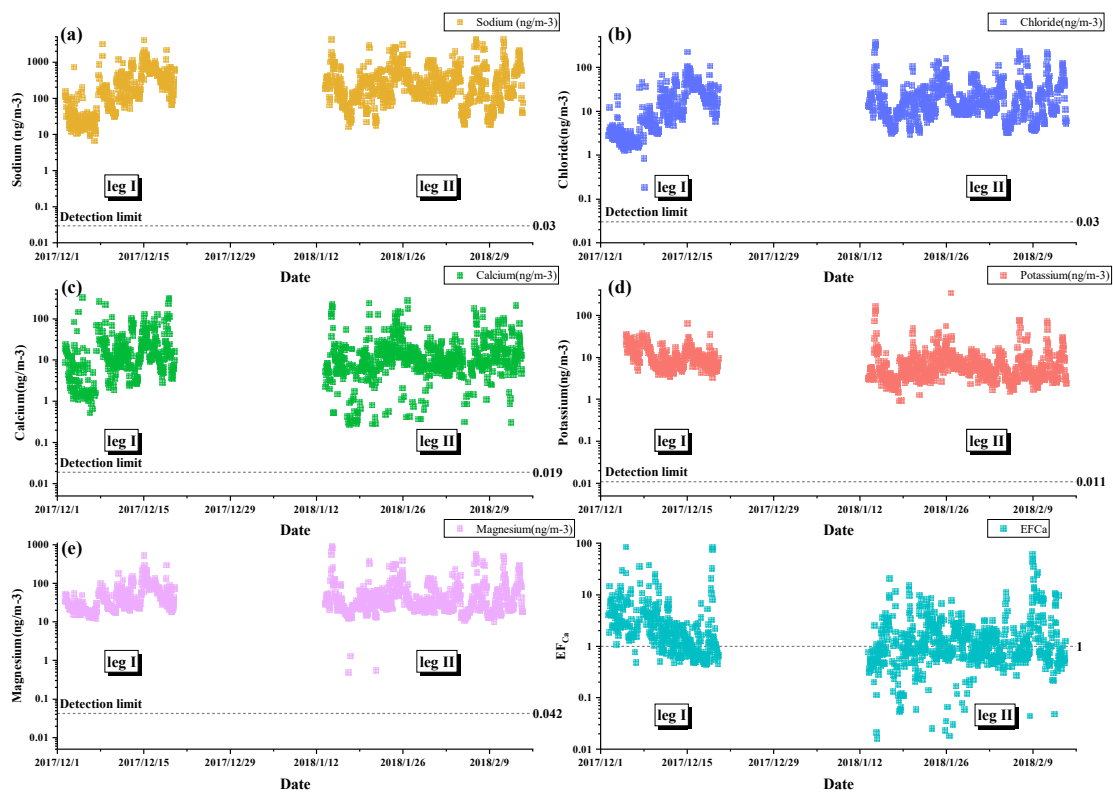
345

346 Figure S13

347 The time series of observed ion mass concentrations and EF_{Ca}.

348
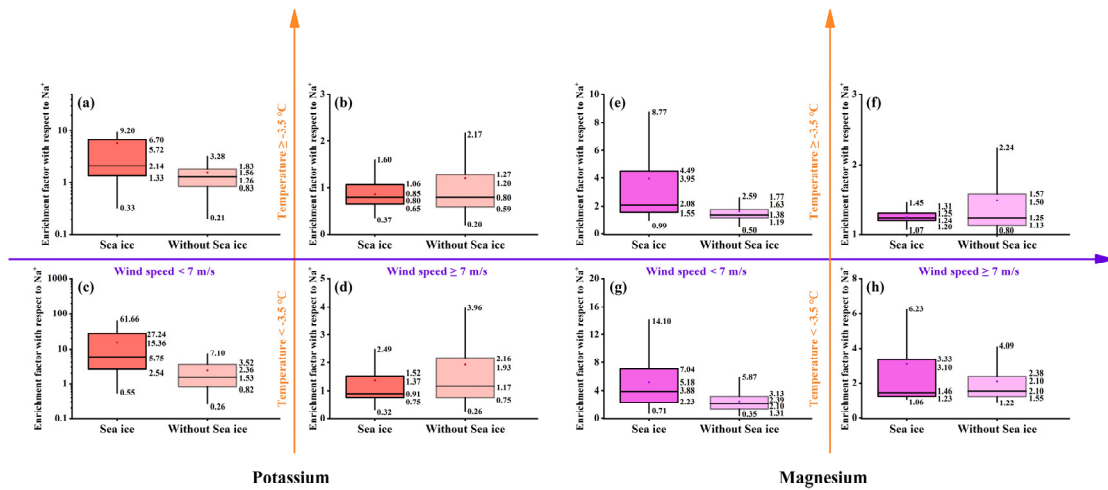
349   Figure S14

350   Box and whisker plots of hourly Ca^{2+} enrichment factor (EF_{Ca}) with respect to Na^+ at different

351   ambient temperatures, wind speeds, and sea ice fraction. In the box and whisker plots, the marked

352   values from top to bottom are the 90th and 75th percentiles, mean, median, and 25th and 10th

353   percentiles, respectively. In comparison with the bubble charts (Fig. S15), the box and whisker plots

354   present similar intensions with different forms.
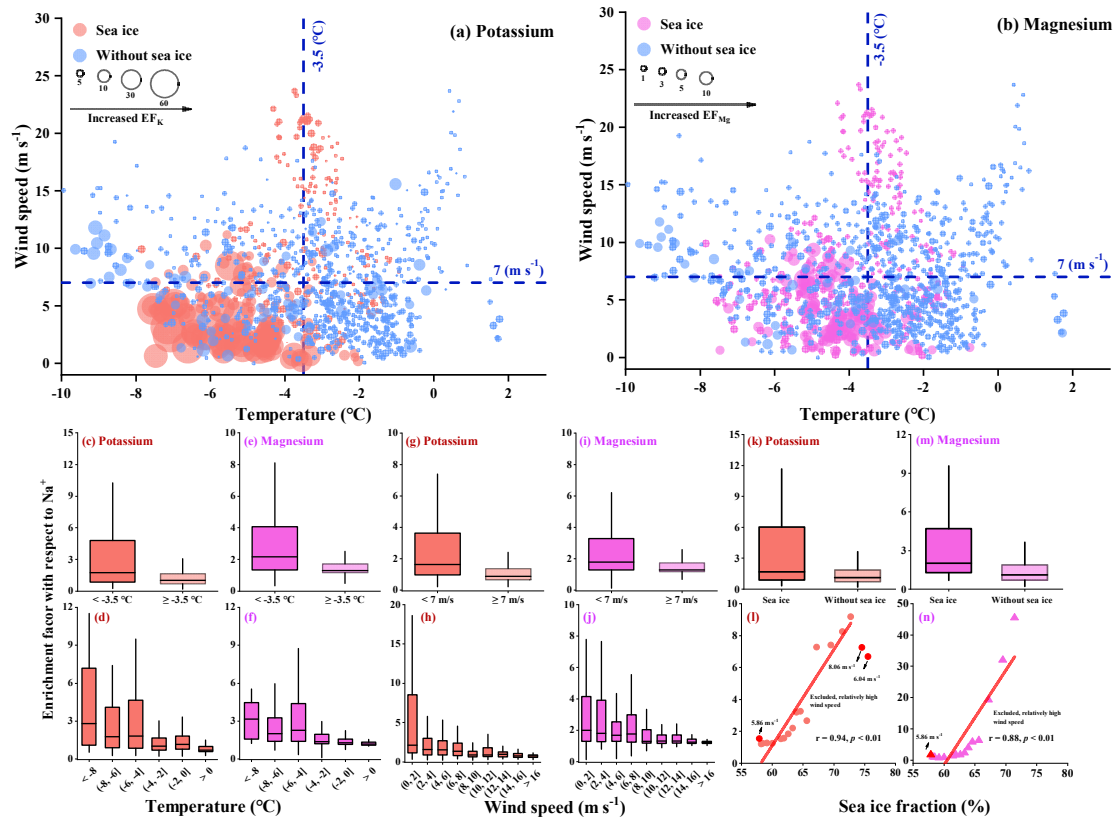
355

356 Figure S15

357 Bubble charts of hourly (a) K$^+$ and (b) Mg^{2+} enrichment factors with respect to Na$^+$ at the ambient

358 temperatures, wind speeds, and sea ice fraction. The enrichment factors of K$^+$ and Mg^{2+} with respect

359 to Na$^+$ varied as a function of the ambient temperature (c-f), wind speed (g-j), and sea ice fraction

360 (k-n) during the cruise observation. In the box and whisker plot, the lower, median, and upper lines

361 of the box denote the 25th, 50th and 75th percentiles, respectively.
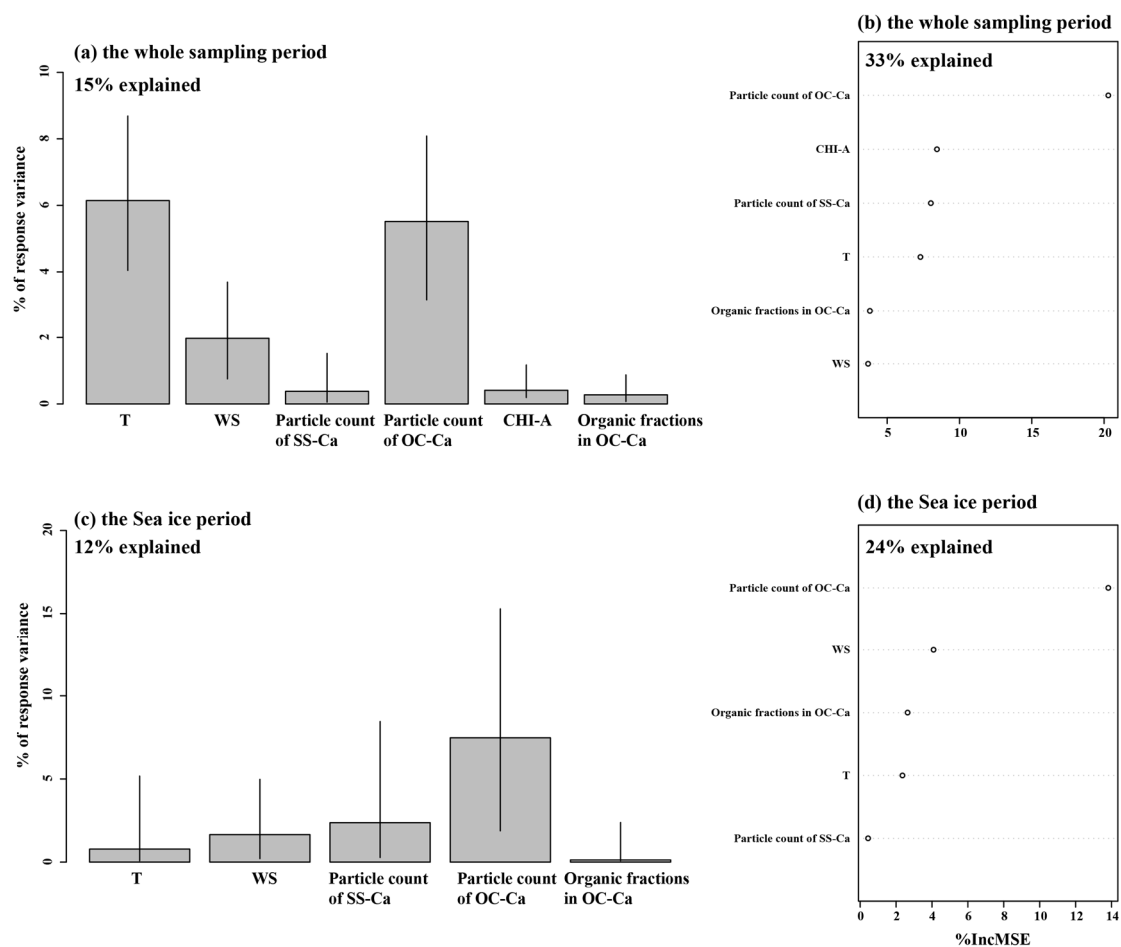
362

363   Figure S16

364   The relative importance to the variation in EF_{Ca}, as determined by multilinear regression for (a) the

365   whole sampling period and (c) the sea ice period. The error bars provide 90% confidence intervals

366   with 100 bootstrap replicates to evaluate the results. The relative importance of the predictors in the

367   random forest analysis for the EF_{Ca} for (b) the whole sampling period and (d) the sea ice period.

368   The %IncMSE, which is used as an indicator for the relative contribution to the predicted variable,

369   refers to the increased mean square-error when each independent variable is removed from the

370   predictors.
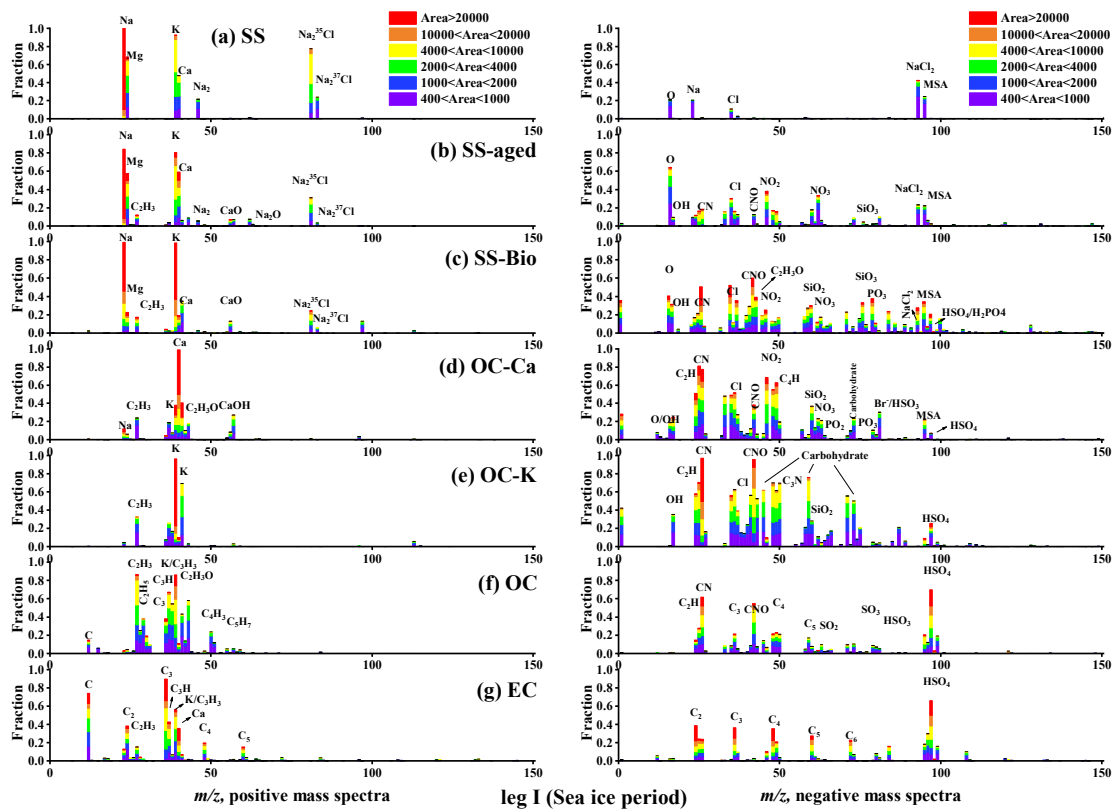
371

Figure S17

Average digitalized single-particle mass spectra for seven classes of collected particles during leg I
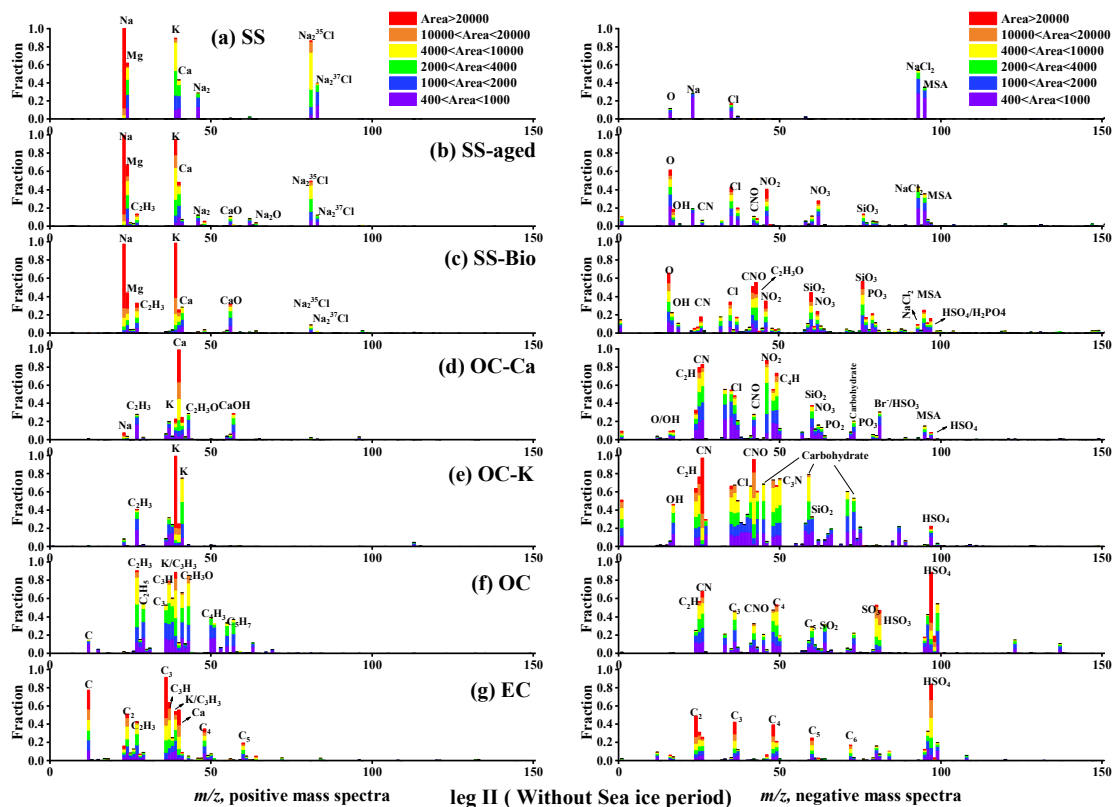
(sea ice period).

375

376   Figure S18

377   Average digitalized single-particle mass spectra for seven classes of collected particles during leg

378   II (period without sea ice).
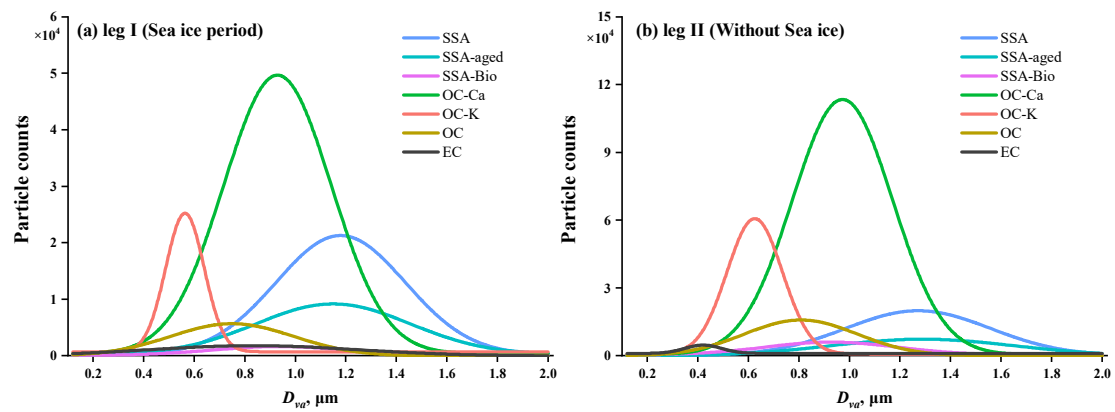
379

380   Figure S19

381   Unscaled size-resolved number distributions of all individual particles during leg I (sea ice period)

382   and leg II (period without sea ice).

(a) Sea ice   **(b) Without Sea ice**
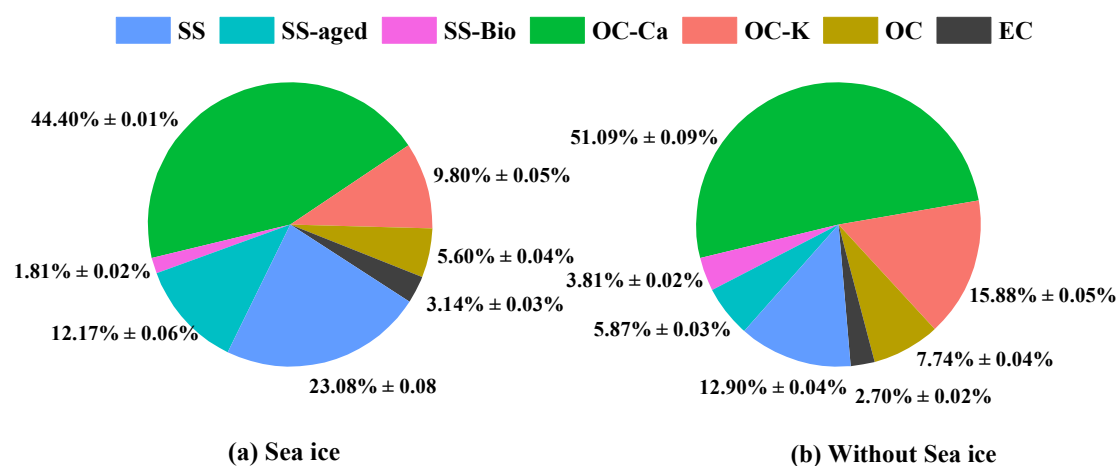
383

384   Figure S20

385   Relative proportion of different single-particle types during leg I (sea ice period) and leg II (period

386   without sea ice). It is still quite a challenge to obtain quantitative measurements using SPAMS due

387   to the potential inhomogeneities in the transmission efficiencies of the aerodynamic lenses and

388   desorption/ionization, and the matrix effects of individual particles (Gross et al., 2000; Qin et al.,

389   2006; Pratt and Prather, 2012). Therefore, it may not be straightforward to use the particle count in

390   comparison with the absolute mass concentration. We noted that there was little difference in OC-

391   Ca proportion during the periods of sea ice and without sea ice. The source of OC-Ca for the two

392   periods may be explained by the low wind-blown sea ice and the blowing-snow from Antarctica

393   (Fig. S1 and Table S1, the influence of air masses from Antarctic land, 40%), respectively. Another

394   reason for that may be the resuspension of OC-Ca. Also, bubble bursts within open water and leads

395   occurred in both periods.
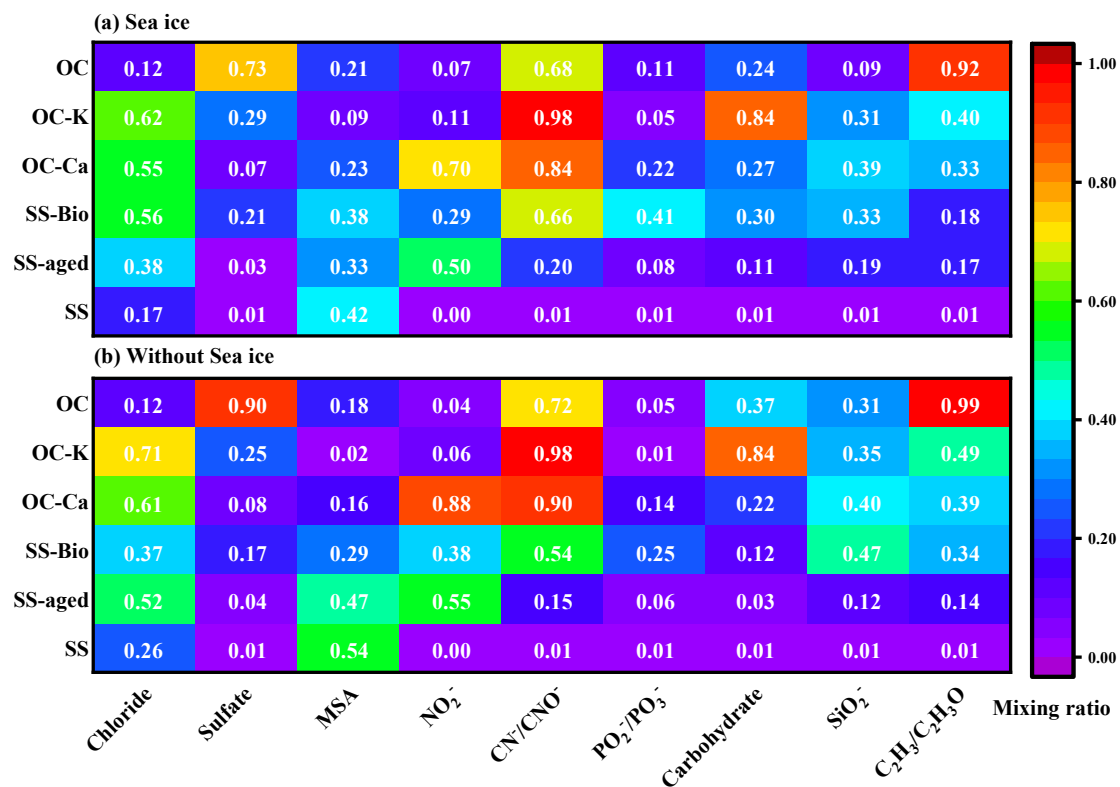
396

397   Figure S21

398   Hot plot of number fractions for major species of obtained single-particle types, including chloride

399   (*m/z* -35 and -37), sulfate (*m/z* -97), methanesulfonic acid (MSA, *m/z* -95), nitro-containing organic

400   species (*m/z* -46), organic nitrogen (*m/z* -26 or -42), phosphate (*m/z* -63 or -79), carbohydrate (*m/z*

401   -45, -59, or -73), siliceous materials (*m/z* -60), and organic carbon (*m/z* -27 or 43). (a) leg I (sea ice

402   period) and leg II (period without sea ice).

403
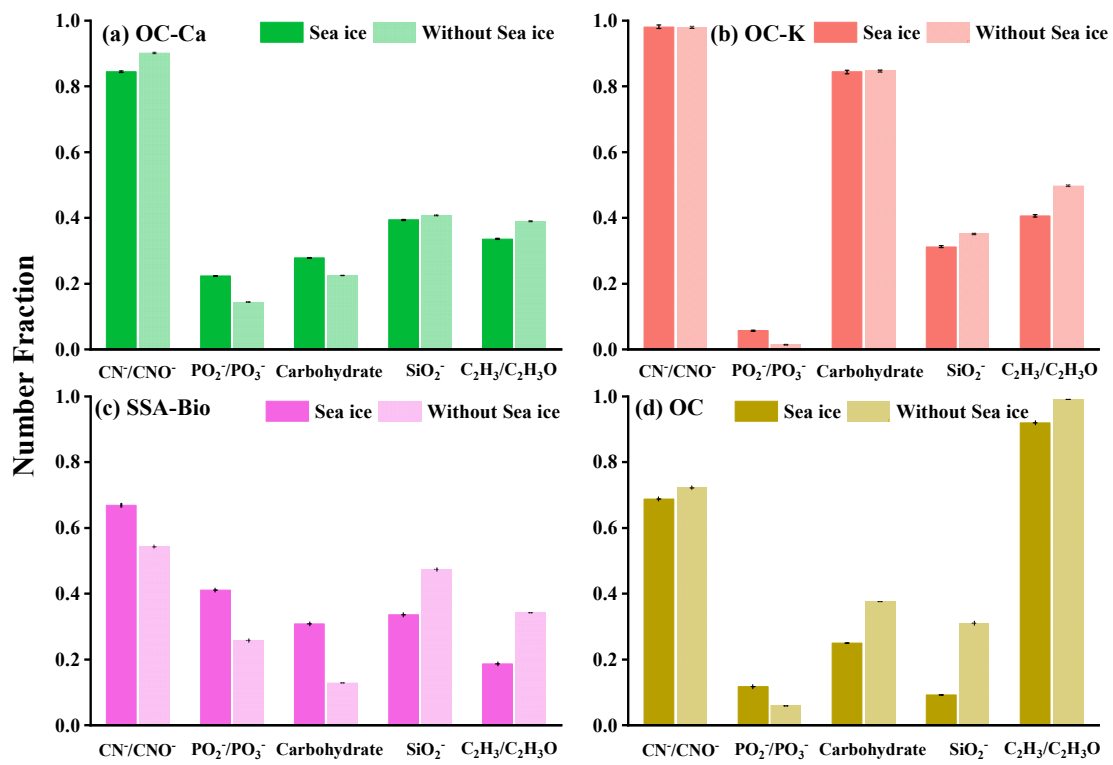
Figure S22

Comparison by number fractions for some typical organic chemical components of (a) OC-Ca, (b)

OC-K, and (c) SS-Bio during leg I (sea ice period) and leg II (period without Sea ice). The errors

are calculated assuming Poisson statistics for the obtained particles.

3. Supplementary Tables

408

no.	Methodology	EF_{Ca}	EF_K	EF_{Mg}	Ref.
1	Laboratory study (fresh and unfiltered seawater)	median = 1.21	n.a.	n.a.	Keene et al. (2007)
2	Field study (Syowa Station, Antarctica)	n.a.	n.a.	1.35-1.55	Hara et al. (2012)
3	Field study (North Atlantic seawater)	~ 100 (45 nm) ~ 10 (80 nm) ~ 4 (150 nm) ~ 2 (200 nm) ~ 1 (500 nm)	~ 5 (45 nm) ~ 1 (80 nm) ~ 1 (150 nm) ~ 1 (200 nm) ~ 1 (500 nm)	~ 2 (45 nm) ~ 1 (80 nm) ~ 1 (150 nm) ~ 1 (200 nm) ~ 1 (500 nm)	Salter et al. (2016)
4	Laboratory study (Artificial seawater)	~ 50 (45 nm) ~ 10 (80 nm) ~ 4 (150 nm) ~ 2.5 (200 nm) ~ 2 (500 nm) ~ 2 (1000 nm)	~ 6 (45 nm) ~ 1 (80 nm) ~ 1 (150 nm) ~ 1 (200 nm) ~ 1 (500 nm) ~ 1 (1000 nm)	~ 2 (45 nm) ~ 1 (80 nm) ~ 1 (150 nm) ~ 1 (200 nm) ~ 1 (500 nm) ~ 1 (1000 nm)	Salter et al. (2016)
5	Laboratory study (Artificial seawater)	~ 5 (56 nm) ~ 1.5 (100 nm) median = 1.14	~ 1.2 (56 nm) ~ 0.3 (100 nm) median = 0.72	~ 1.1 (56 nm) ~ 1 (100 nm) median = 0.83	Cochran et al. (2016)
6	Field study (Arctic Ocean)	geometric mean = 3.7 (from 1.2 to 39)	1 - 8	0.1 - 1	Mukherjee et al. (2020)
7	Field study (the Ross Sea, Southern Ocean)	0.01 - 85, median = 2.76, mean = 1.18	0.20 - 75, median = 3.61, mean = 1.19	0.12 - 26.94, median = 2.46, mean = 1.48	This study

n.a. refers that the value was unavailable.

Note: Enrichment factors of a specific species X with respect to sodium (EF_x) are defined as the ratio of the mass concentration of a specific species X to the mass concentration of sodium in the particle to the same ratio in bulk seawater.

409   Table S1

410   A comparative analysis of enrichment factors of a specific species X (EF_X, in which X indicates

411   Ca^{2+}, K^+, and Mg^{2+}) with respect to sodium between previous studies and this study.

412

Item	leg1 (02.12.2017-20.12.2017)	leg2 (13.01.2018-14.02.2018)	The whole observation
Na (ng m^{-3})	306.72 ± 421.77	395.84 ± 561.04	364.64 ± 561.04
Ca (ng m^{-3})	24.54 ± 41.28	19.38 ± 30.80	21.20 ± 34.96
K (ng m^{-3})	11.39 ± 7.33	8.72 ± 17.65	9.54 ± 15.28
Mg (ng m^{-3})	50.63 ± 48.67	59.61 ± 88.89	56.59 ± 77.47
Cl (ng m^{-3})	18.16 ± 22.18	26.57 ± 36.85	23.63 ± 32.74
EF$_{Ca}$	3.94 ± 8.50	2.11 ± 4.47	2.76 ± 6.27
Positive calcium enrichment event (%)	71.0%	47.7%	56.0%
EF$_{K}$	7.93 ± 14.03	1.67 ± 1.69	3.61 ± 8.45
Positive potassium enrichment event (%)	67.9%	54.2%	58.4%
EF$_{Mg}$	3.74 ± 3.75	1.80 ± 1.05	2.46 ± 2.53
Positive magnesium enrichment event (%)	99.0%	95.2%	96.3%
Temperature (℃)	-4.1 ± 1.4	-3.2 ± 2.2	-3.5 ± 2.0
Wind speed (m s^{-1})	7.2 ± 5.5	7.1 ± 4.2	7.1 ± 4.7
Sea ice fraction	64.91 ± 5.57	54.59 ± 0.08	58.38 ± 6.07
ChI-a concentration (μg L^{-1})	0.51 ± 0.29	0.44 ± 0.18	0.46 ± 0.23
72-Trajectory coverage (%) Sea ice: Open water: Antarctic Land:	78% 6% 16%	28% 32% 40%	48% 21% 31%

Note: During the leg I, the sea ice was retreat. During the leg II, almost no sea ice coverage is equivalent to the sea ice fraction below 55.

413

414   Table S2

415   Average measured ion mass concentrations, enrichment factors for specific cations, and

416   metrological parameters for leg I and leg II.

Particle types	Major peaks	Particle count		Total particle count
		leg1 (02.12.2017-20.12.2017)	leg2 (13.01.2018-14.02.2018)	
SSA	$[Na]^+$, $[Na_2]^+$, $[Na^2Cl]^+$, $[Mg]^{2+}$, $[K]+$, $[Ca]^{2+}$, and $[Cl]^-$	69982	71930	141912
SSA-aged	Inorganic salt signature and nitrate of $[NO_2]-$ and $[NO_3]^-$	36905	32741	69646
SSA-Bio	Inorganic salt signature and organic matter signals	5489	21276	26765
OC-Ca	$[Ca]^{2+}$ and organic matter signals	134653	284861	419514
OC-K	$[K]^+$ and organic matter signals	29734	88549	118283
OC	Organic matter signals	16980	88549	105529
EC	Element carbon with m/z $\pm C_n$, n = 1 - 6	9515	15036	24551

Inorganic salt signatures: $[Na]^+$, $[Na_2]^+$, $[Na_2Cl]^+$, $[Mg]^{2+}$, $[K]^+$, $[Ca]^{2+}$, and $[Cl]^-$.

Organic matter signals: organic nitrogen ($[CN]^-$ and $[CNO]^-$), phosphate ($[PO_2]-$ and $[PO_3]-$), carbohydrate ($[CHO_2]^-$, $[C_2H_3O_2]^-$, and $[C_3H_5O_2]^-$), siliceous materials ($[SiO_2]^-$), and organic carbon ($[C_2H_3]^+$ and $[C_2H_3O_3]^+$).

417

418   Table S3

419   Particle counts and characteristic peaks for the seven single-particle chemical classes obtained

420   during cruise observations.

Item	Area 1 (2018.02.08 19:00- 2017.02.10 18:00)	Area 2 (2018.01.22 16:00- 2018.01.24 01:00)	Area 3 (2017.12.02 07:00- 2017.12.04 19:00)	Area 4 (2017.12.05 00:00- 2017.12.05 23:00)	Area 5 (2017.12.18 20:00-2017.12.19 03:00)	leg I	leg II	The whole observation
EF_{Ca}	10.73 ± 13.63	3.98 ± 1.84	5.47 ± 4.64	9.72 ± 18.75	30.98 ± 31.32	3.94 ± 8.50	2.11 ± 4.47	2.76 ± 6.27
EF_{K}	2.88 ± 2.36	1.72 ± 0.79	n.a.	45.46 ± 14.79	1.22 ± 0.46	7.93 ± 14.03	1.67 ± 1.69	3.61 ± 8.45
EF_{Mg}	2.88 ± 1.54	2.24 ± 0.63	7.89 ± 4.35	8.25 ± 2.90	1.38 ± 0.33	3.74 ± 3.75	1.80 ± 1.05	2.46 ± 2.53
Temperature (℃)	-6.4 ± 1.2	-2.8 ± 0.6	-4.5 ± 0.9	-4.0 ± 0.8	-1.9 ± 2.2	-4.1 ± 1.4	-3.2 ± 2.2	-3.5 ± 2.0
Wind speed (m s^{-1})	5.7 ± 3.5	4.5 ± 1.9	6.04 ± 2.2	2.49 ± 1.1	5.1 ± 4.5	7.2 ± 5.5	7.1 ± 4.2	7.1 ± 4.7
Sea ice fraction	54.60 ± 0.02	54.53 ± 0.00	74.28 ± 1.41	71.41	58.06 ± 0.25	64.91 ± 5.57	54.59 ± 0.08	58.38 ± 6.07
ChI-a concentration (μg L^{-1})	0.99 ± 1.65	0.10± 0.20	Unavailable	Unavailable	Unavailable	0.51 ± 0.29	0.44 ± 0.18	0.46 ± 0.23
72-Trajectory coverage (%)* Sea ice: Open water: Antarctic Land:	2% 0% 98%	1% 0% 99%	100% 0% 0%	100% 0% 0%	76% 22% 2%	78% 6% 16%	28% 32% 40%	48% 21% 31%

Note: (1) Area 1 and 2 are divided during the leg II, whereas the Area 3, 4, and 5 are divided during the leg I. (2) The values of sea ice intensity and chI-a concentration present with daily resolution. Others present with hourly resolution. (3) No sea ice coverage is equivalent to the sea ice fraction below 55. (4) 72-Trajectory coverage (%)* correspounds to fraction of air masses traveled over different surface type when the peak EFCa value from Area 1 to 5. For leg I, II, and the whole observation, this fraction was calcluated with daily resolution.

Table S4

Average enrichment factors for specific cations and metrological parameters over the different areas mentioned in Fig. S7. Although all of these areas exhibited significant Ca^{2+} enrichment in SSAs, they may have varied due to synergetic environmental factors rather than a single factor. Ca^{2+} enrichment in SSA was notably observed with low wind speed, underscoring the effect of wind speed. The back trajectories are labeled as sea ice, open water, and land, disregarding periods that the air mass spent above the mixed layer height.

For the leg I, the major positive Ca^{2+} enrichment events were associated with Areas 3, 4, and 5. In addition to the lower wind speed, lower temperature, and the presence of sea ice, the air masses blew over the large fraction of sea-ice-covered ocean may play an important role in Ca^{2+} enrichment.

For the leg II, the major positive Ca^{2+} enrichment events were occurred in Areas 1 and 2, which mainly associated with lower wind speed and temperature. The air masses were mostly from the snow-covered Antarctic land.

EF_{Ca}	Count (Correlation coefficient, r)				Peak area (Correlation coefficient, r, m/z 40 $[Ca]^{2+}$)			
	OC-Ca-Inorganic	OC-Ca-Organic	OC-Ca	SS-Ca	OC-Ca-Inorganic	OC-Ca-Organic	OC-Ca	SS-Ca
0 - 5	0.08	0.31	0.18	0.07	0.18	0.44	0.41	0.04
5 - 10	0.15	0.37	0.27	0.04	0.14	0.36	0.33	0.06
> 10	0.58	0.59	0.63	0.10[a]	0.53	0.68	0.68	0.10
Total	0.28	0.51	0.42	0.21	0.31	0.51	0.49	0.03

436   a: p-value > 0.05

437   Table S5

438   Correlation analysis between the OC-Ca (by count and by peak area of m/z 40 $[Ca]^+$) and its two

439   subpopulations OC-Ca-Organic and OC-Ca-Inorganic, SS-Ca (by count and by peak area of m/z 40

440    $[Ca]^+$), and mass concentration of Ca^{2+} in the variation of EF_{Ca}, with the p-value < 0.05.

441

References

Boreddy, S. K. R. and Kawamura, K.: A 12-year observation of water-soluble ions in TSP aerosols collected at a remote marine location in the western North Pacific: an outflow region of Asian dust, Atmos Chem Phys, 15, 6437-6453, https://doi.org/10.5194/acp-15-6437-2015, 2015.

Cochran, R. E., Jayarathne, T., Stone, E. A., and Grassian, V. H.: Selectivity Across the Interface: A Test of Surface Activity in the Composition of Organic-Enriched Aerosols from Bubble Bursting, J Phys Chem Lett, 7, 1692-1696, https://doi.org/10.1021/acs.jpclett.6b00489, 2016.

Cochran, R. E., Laskina, O., Trueblood, J. V., Estillore, A. D., Morris, H. S., Jayarathne, T., Sultana, C. M., Lee, C., Lin, P., Laskin, J., Laskin, A., Dowling, J. A., Qin, Z., Cappa, C. D., Bertram, T. H., Tivanski, A. V., Stone, E. A., Prather, K. A., and Grassian, V. H.: Molecular Diversity of Sea Spray Aerosol Particles: Impact of Ocean Biology on Particle Composition and Hygroscopicity, Chem., 2, 655-667, https://doi.org/10.1016/j.chempr.2017.03.007, 2017.

Collins, D. B., Zhao, D. F., Ruppel, M. J., Laskina, O., Grandquist, J. R., Modini, R. L., Stokes, M. D., Russell, L. M., Bertram, T. H., Grassian, V. H., Deane, G. B., and Prather, K. A.: Direct aerosol chemical composition measurements to evaluate the physicochemical differences between controlled sea spray aerosol generation schemes, Atmos Meas Tech, 7, 3667-3683, https://doi.org/10.5194/amt-7-3667-2014, 2014.

Facchini, M. C., Rinaldi, M., Decesari, S., Carbone, C., Finessi, E., Mircea, M., Fuzzi, S., Ceburnis, D., Flanagan, R., Nilsson, E. D., de Leeuw, G., Martino, M., Woeltjen, J., and O'Dowd, C. D.: Primary submicron marine aerosol dominated by insoluble organic colloids and aggregates, Geophys Res Lett, 35https://doi.org/10.1029/2008gl034210, 2008.

Gaston, C. J., Furutani, H., Guazzotti, S. A., Coffee, K. R., Bates, T. S., Quinn, P. K., Aluwihare, L. I., Mitchell, B. G., and Prather, K. A.: Unique ocean-derived particles serve as a proxy for changes in ocean chemistry, Journal of Geophysical Research: Atmospheres, 116https://doi.org/10.1029/2010jd015289, 2011.

Gross, D. S., Galli, M. E., Silva, P. J., and Prather, K. A.: Relative sensitivity factors for alkali metal and ammonium cations in single particle aerosol time-of-flight mass spectra, Anal Chem, 72, 416-422, https://doi.org/10.1021/ac990434g, 2000.

Guasco, T. L., Cuadra-Rodriguez, L. A., Pedler, B. E., Ault, A. P., Collins, D. B., Zhao, D. F., Kim, M. J., Ruppel, M. J., Wilson, S. C., Pomeroy, R. S., Grassian, V. H., Azam, F., Bertram, T. H., and Prather, K. A.: Transition Metal Associations with Primary Biological Particles in Sea Spray Aerosol Generated in a Wave Channel, Environ Sci Technol, 48, 1324-1333, https://doi.org/10.1021/es403203d, 2014.

Hara, K., Osada, K., Yabuki, M., and Yamanouchi, T.: Seasonal variation of fractionated sea-salt particles on the Antarctic coast, Geophys Res Lett, 39https://doi.org/10.1029/2012gl052761, 2012.

Healy, R. M., Sciare, J., Poulain, L., Kamili, K., Merkel, M., Muller, T., Wiedensohler, A., Eckhardt, S., Stohl, A., Sarda-Esteve, R., McGillicuddy, E., O'Connor, I. P., Sodeau, J. R., and Wenger, J. C.: Sources and mixing state of size-resolved elemental carbon particles in a European megacity: Paris, Atmos Chem Phys, 12, 1681-1700, https://doi.org/10.5194/acp-12-1681-2012, 2012.

Keene, W. C., Maring, H., Maben, J. R., Kieber, D. J., Pszenny, A. A. P., Dahl, E. E., Izaguirre, M. A., Davis, A. J., Long, M. S., Zhou, X. L., Smoydzin, L., and Sander, R.: Chemical and physical characteristics of nascent aerosols produced by bursting bubbles at a model air-sea interface, Journal of Geophysical Research: Atmospheres, 112https://doi.org/10.1029/2007jd008464, 2007.

Leck, C. and Bigg, E. K.: New Particle Formation of Marine Biological Origin, Aerosol Sci Tech, 44, 570-577, https://doi.org/10.1080/02786826.2010.481222, 2010.

Li, L., Huang, Z., Dong, J., Li, M., Gao, W., Nian, H., Fu, Z., Zhang, G., Bi, X., Cheng, P., and Zhou, Z.: Real time bipolar time-of-flight mass spectrometer for analyzing single aerosol particles, Int J Mass Spectrom, 303, 118-124, https://doi.org/10.1016/j.ijms.2011.01.017, 2011.

Lundberg, S. M., Erion, G., Chen, H., DeGrave, A., Prutkin, J. M., Nair, B., Katz, R., Himmelfarb, J., Bansal, N., and Lee, S. I.: From local explanations to global understanding with explainable AI for trees, Nat Mach Intell, 2, 56-67, https://doi.org/10.1038/s42256-019-0138-9, 2020.

Mukherjee, P., Reinfelder, J. R., and Gao, Y.: Enrichment of calcium in sea spray aerosol in the Arctic summer atmosphere, Mar Chem, 227https://doi.org/10.1016/j.marchem.2020.103898, 2020.

Oppo, C., Bellandi, S., Innocenti, N. D., Stortini, A. M., Loglio, G., Schiavuta, E., and Cini, R.: Surfactant components of marine organic matter as agents for biogeochemical fractionation and pollutant transport via marine aerosols, Mar Chem, 63, 235-253, https://doi.org/10.1016/S0304-4203(98)00065-6, 1999.

Orellana, M. V. and Verdugo, P.: Ultraviolet radiation blocks the organic carbon exchange between the dissolved phase and the gel phase in the ocean, Limnol Oceanogr, 48, 1618-1623, https://doi.org/10.4319/lo.2003.48.4.1618, 2003.

Orellana, M. V., Matrai, P. A., Leck, C., Rauschenberg, C. D., Lee, A. M., and Coz, E.: Marine microgels as a source of cloud condensation nuclei in the high Arctic, P Natl Acad Sci USA, 108, 13612-13617, https://doi.org/10.1073/pnas.1102457108, 2011.

Prather, K. A., Bertram, T. H., Grassian, V. H., Deane, G. B., Stokes, M. D., DeMott, P. J., Aluwihare, L. I., Palenik, B. P., Azam, F., Seinfeld, J. H., Moffet, R. C., Molina, M. J., Cappa, C. D., Geiger, F. M., Roberts, G. C., Russell, L. M., Ault, A. P., Baltrusaitis, J., Collins, D. B., Corrigan, C. E., Cuadra-Rodriguez, L. A., Ebben, C. J., Forestieri, S. D., Guasco, T. L., Hersey, S. P., Kim, M. J., Lambert, W. F., Modini, R. L., Mui, W., Pedler, B. E., Ruppel, M. J., Ryder, O. S., Schoepp, N. G., Sullivan, R. C., and Zhao, D. F.: Bringing the ocean into the laboratory to probe the chemical complexity of sea spray aerosol, P Natl Acad Sci USA, 110, 7550-7555, https://doi.org/10.1073/pnas.1300262110, 2013.

Pratt, K. A. and Prather, K. A.: Mass spectrometry of atmospheric aerosolsuRecent developments and applications. Part II: On-line mass spectrometry techniques, Mass Spectrom Rev, 31, 17-48, https://doi.org/10.1002/mas.20330, 2012.

Qin, X. Y., Bhave, P. V., and Prather, K. A.: Comparison of two methods for obtaining quantitative mass concentrations from aerosol time-of-flight mass spectrometry measurements, Anal Chem, 78, 6169-6178, https://doi.org/10.1021/ac060395q, 2006.

Quinn, P. K., Collins, D. B., Grassian, V. H., Prather, K. A., and Bates, T. S.: Chemistry and Related Properties of Freshly Emitted Sea Spray Aerosol, Chem Rev, 115, 4383-4399, https://doi.org/10.1021/cr500713g, 2015.

Salter, M. E., Hamacher-Barth, E., Leck, C., Werner, J., Johnson, C. M., Riipinen, I., Nilsson, E. D., and Zieger, P.: Calcium enrichment in sea spray aerosol particles, Geophys Res Lett, 43, 8277-8285, https://doi.org/10.1002/2016gl070275, 2016.

Schill, S. R., Collins, D. B., Lee, C., Morris, H. S., Novak, G. A., Prather, K. A., Quinn, P. K., Sultana, C. M., Tivanski, A. V., Zimmermann, K., Cappa, C. D., and Bertram, T. H.: The Impact of Aerosol Particle Mixing State on the Hygroscopicity of Sea Spray Aerosol, Acs Central Sci, 1, 132-141, https://doi.org/10.1021/acscentsci.5b00174, 2015.

Schlitzer, R.: Interactive analysis and visualization of geoscience data with Ocean Data View, Comput Geosci-Uk, 28, 1211-1218, https://doi.org/10.1016/S0098-3004(02)00040-7, 2002.

Sierau, B., Chang, R. Y. W., Leck, C., Paatero, J., and Lohmann, U.: Single-particle characterization of the high-Arctic summertime aerosol, Atmos Chem Phys, 14, 7409-7430, https://doi.org/10.5194/acp-14-7409-2014, 2014.

Song, C., Becagli, S., Beddows, D. C. S., Brean, J., Browse, J., Dai, Q., Dall'Osto, M., Ferracci, V., Harrison, R. M., Harris, N., Li, W., Jones, A. E., Kirchgäßner, A., Kramawijaya, A. G., Kurganskiy, A., Lupi, A., Mazzola, M., Severi, M., Traversi, R., and Shi, Z.: Understanding Sources and Drivers of Size-Resolved Aerosol in the High Arctic Islands of Svalbard Using a Receptor Model Coupled with Machine Learning, Environ Sci Technol, 56, 11189-11198, https://doi.org/10.1021/acs.est.1c07796, 2022.

Su, B., Wang, T., Zhang, G., Liang, Y., Lv, C., Hu, Y., Li, L., Zhou, Z., Wang, X., and Bi, X.: A review of atmospheric aging of sea spray aerosols: Potential factors affecting chloride depletion, Atmos Environ, 290https://doi.org/10.1016/j.atmosenv.2022.119365, 2022.

Su, B. J., Zhang, G. H., Zhuo, Z. M., Xie, Q. H., Du, X. B., Fu, Y. Z., Wu, S., Huang, F. G., Bi, X. H., Li, X., Li, L., and Zhou, Z.: Different characteristics of individual particles from light-duty diesel vehicle at the launching and idling state by AAC-SPAMS, Journal of Hazardous Materials, 418https://doi.org/10.1016/j.jhazmat.2021.126304, 2021a.

Su, B. J., Zhuo, Z. M., Fu, Y. Z., Sun, W., Chen, Y., Du, X. B., Yang, Y. X., Wu, S., Xie, Q. H., Huang, F. G., Chen, D. H., Li, L., Zhang, G. H., Bi, X. H., and Zhou, Z.: Individual particle investigation on the chloride depletion of inland transported sea spray aerosols during East Asian summer monsoon, Sci Total Environ, 765https://doi.org/10.1016/j.scitotenv.2020.144290, 2021b.

Yan, J., Jung, J., Lin, Q., Zhang, M., Xu, S., and Zhao, S.: Effect of sea ice retreat on marine aerosol emissions in the Southern Ocean, Antarctica, Sci Total Environ, 745, 140773, https://doi.org/10.1016/j.scitotenv.2020.140773, 2020a.

Yan, J., Jung, J., Zhang, M., Xu, S., Lin, Q., Zhao, S., and Chen, L.: Significant Underestimation of Gaseous Methanesulfonic Acid (MSA) over Southern Ocean, Environ Sci Technol, 53, 13064-13070, https://doi.org/10.1021/acs.est.9b05362, 2019.

Yan, J., Jung, J., Zhang, M., Bianchi, F., Tham, Y., Xu, S., Lin, Q., Zhao, S., Li, L., and Chen, L.: Uptake selectivity of methanesulfonic acid (MSA) on fine particles over polynya regions of the Ross Sea, Antarctica, Atmos Chem Phys, 20, 3259-3271, https://doi.org/10.5194/acp-20-3259-2020, 2020b.

Zhang, G., Fu, Y., Peng, X., Sun, W., Shi, Z., Song, W., Hu, W., Chen, D., Lian, X., Li, L., Tang, M., Wang, X., and Bi, X.: Black Carbon Involved Photochemistry Enhances the Formation of Sulfate in the Ambient Atmosphere: Evidence From In Situ Individual Particle Investigation, Journal of Geophysical Research: Atmospheres, 126https://doi.org/10.1029/2021jd035226, 2021.